Early-Pleistocene orbital variability in Northwest Australian shelf s

Song Zhao[1], Katharine Grant[1], David Heslop[1], and Stephen J. Gallagher[2]

[1]Research School of Earth Sciences, the Australian National University
[2]School of Geography, Earth and Atmospheric Sciences, University of Melbourne

December 12, 2023

Abstract

Paleoclimate proxy records from regions sensitive to humidity/aridity extremes provide valuable insights into natural forcing mechanisms underlying long-term climate variability in the wider region. One such area is Northwest Australia, where the Australian monsoon impacts its northernmost fringes, which are bordered by the Great Sandy Desert inland. Marine sediments from the Australian Northwest Shelf record fluvial run-off and aeolian dust input during the wet and dry seasons. The location is therefore ideal for investigating long-term variability in the Australian monsoon and Northwest Australian dust fluxes over orbital timescales. However, there are few continuous, high-resolution paleoclimate records from the Australian Northwest Shelf spanning the Early Pleistocene, and there is ambiguous orbital phasing even among Late Pleistocene paleoclimate records from the region. Here, we present geochemical and environmental magnetic proxy records of $CaCO_3$ and dust-flux variability spanning 2.9 to 1.6 Myr ago from International Ocean Discovery Program Expedition 356 Site U1464 on the Australian Northwest Shelf. We establish a new, orbitally-tuned chronology for Site U1464, and observe strong obliquity variability (41 kyr and 54 kyr periodicities) but almost no precession signal in our dust records. We propose that the 41 kyr cycle in Northwest Australian dust fluxes could be a linear response to the East Asian winter monsoon (EAWM) and/or summer inter-tropical insolation gradient (SITIG), whereas the 54 kyr cyclicity might be a non-linear response to obliquity amplitude modulation via the SITIG effect on cross-equatorial flows.

Early-Pleistocene orbital variability in Northwest Australian shelf sediments

Song Zhao[1*], Katharine M. Grant[1], David Heslop[1], and Stephen J. Gallagher[2]

[1] Research School of Earth Sciences, Australian National University, Canberra, ACT, Australia.

[2] School of Geography, Earth and Atmospheric Sciences, University of Melbourne, Melbourne, Victoria, Australia.

*Corresponding author: Song Zhao (zhaosong8501555@163.com)

Key Points:

- This study establishes a new orbitally-constrained chronology for IODP Site U1464.
- Northwest Australian shelf sediments preserve ~400 kyr eccentricity cyclicity in $CaCO_3$ content and obliquity cycles in dust proxy records.
- Obliquity in Northwest Australian dust fluxes may be related to the East Asian winter monsoon and summer inter-tropical insolation gradient.

Abstract

Paleoclimate proxy records from regions sensitive to humidity/aridity extremes provide valuable insights into natural forcing mechanisms underlying long-term climate variability in the wider region. One such area is Northwest Australia, where the Australian monsoon impacts its northernmost fringes, which are bordered by the Great Sandy Desert inland. Marine sediments from the Australian Northwest Shelf record fluvial run-off and aeolian dust input during the wet and dry seasons. The location is therefore ideal for investigating long-term variability in the Australian monsoon and Northwest Australian dust fluxes over orbital timescales. However, there are few continuous, high-resolution paleoclimate records from the Australian Northwest Shelf spanning the Early Pleistocene, and there is ambiguous orbital phasing even among Late Pleistocene paleoclimate records from the region. Here, we present geochemical and environmental magnetic proxy records of $CaCO_3$ and dust-flux variability spanning 2.9 to 1.6 Myr ago from International Ocean Discovery Program Expedition 356 Site U1464 on the Australian Northwest Shelf. We establish a new, orbitally-tuned chronology for Site U1464, and observe strong obliquity variability (41 kyr and 54 kyr periodicities) but almost no precession signal in our dust records. We propose that the 41 kyr cycle in Northwest Australian dust fluxes could be a linear response to the East Asian winter monsoon (EAWM) and/or summer inter-tropical insolation gradient (SITIG), whereas the 54 kyr cyclicity might be a non-linear response to obliquity amplitude modulation via the SITIG effect on cross-equatorial flows.

1. Introduction

Sediments from the Australian Northwest Shelf (NWS) contain a valuable archive of past Australian monsoon variability, as well as dust fluxes from the Australian interior. Fluvial transport of terrigenous materials to the NWS occurs during the wet season (mainly December to March), primarily from the Ord and Fitzroy Rivers in the far north, and from the De Grey and Fortescue Rivers at the southern margin of the NWS (Australia's River Basins, 1997) (Figure 1, Figure S1). In contrast, aeolian dust fluxes to the Australian NWS mostly occur in austral spring to autumn (September to May), when aeolian dust is transported by frontal systems and southeasterly trade winds from Lake Eyre Basin through Northwest Australia to the NWS (Baddock et al., 2015; Ekström et al., 2004; Gallagher & deMenocal, 2019; McGowan & Clark, 2008; McTainsh, 1989; Strong et al., 2011). This seasonal pattern of precipitation and dust flux is therefore tightly linked to insolation changes and the latitudinal position of the Intertropical Convergence Zone (ITCZ), based on modern observations that seasonal migrations of insolation maxima and the ITCZ are strongly coupled with rainfall and southeasterly trade winds in Northwest Australia (Suppiah, 1992). However, over longer timescales, the relationship between insolation/orbital forcing and Australian monsoon and dust-flux variability is not well known. For example, Australian monsoon strength might either respond to local insolation dominated by precession (Holbourn et al., 2005; Liu et al., 2015; Pei et al., 2021) or to Northern Hemisphere insolation changes driven by precession and obliquity (Magee et al., 2004). These different suggested phasings of the Australian monsoon with orbital forcing could, at least in part, be attributed to fluctuations in global ice volume/sea level. Many studies have reported evidence of increased dust fluxes to the Australian NWS (Courtillat et al., 2020; Hesse et al., 2004; Pei et al., 2021; Stuut et al., 2014, 2019) and decreased Australian monsoonal precipitation (Gallagher et al., 2014; Gallagher & Wagstaff, 2021; Kershaw et al., 2003; Magee et al., 2004; Miller et al., 2018; Stuut et al., 2014, 2019) during glacials and/or stadials, while other studies have interpreted intensified Australian monsoonal precipitation during glacials and/or stadials as a response to southward migration of the ITCZ (Bayon et al., 2017; Denniston et al., 2017; Fu et al., 2017).

One of the main issues is that there are few continuous, high-resolution paleoclimate records from this region spanning multiple glacial-interglacial cycles, especially those that extend back to the Early Pleistocene. Of the available high-resolution records, most tend to be focused on periods within the last glacial cycle (the last ~130 kyr), when the effects of millennial climate variability and/or the last deglaciation obfuscate the primary response of Australian monsoon and Northwest Australian dust fluxes to direct orbital forcing (Bayon et al., 2017; Denniston et al., 2017; Fu et al., 2017; Miller et al., 2018). Longer suitable paleoclimate records extending over >1 million years (Myr) exist but are fewer, and their interpretations are more focused on long-term trends (Christensen et al., 2017; Stuut et al., 2019). For example, proxy records of past dust fluxes based on sedimentary Th/K at International Ocean Discovery program (IODP) Site U1463 (Christensen et al., 2017) and Log(Zr/Fe) at Ocean Drilling Program (ODP) Site 762 (Stuut et al., 2019) have been used to investigate the Pliocene-Pleistocene evolution of Northwest Australian aridity. These studies found increasingly greater variance in aridity from the Pliocene to Pleistocene.

Modelling studies of Australian monsoon variability over orbital timescales are relatively rare. Earlier studies suggested a direct response of Australian summer monsoon precipitation to local insolation (Chappell & Syktus, 1996; Wyrwoll & Valdes, 2003; Wyrwoll et al., 2007), or to Northern Hemisphere insolation via cross-equatorial flow (Miller et al., 2005), but these simulations were limited by modelling capacity at that time, such as low-resolution grids and lacking many feedback processes. More recent model simulations of Australian monsoon variability over orbital timescales suggest that obliquity plays a greater role than expected from its smaller insolation contribution relative to precession, and that higher obliquity could result in stronger summer monsoons in Northwest Australia via a stronger pressure gradient between intensified Siberian High and Australian Low pressure cells (Liu et al., 2015; Shi et al., 2011; Wyrwoll et al., 2007). The interpreted obliquity forcing in simulations, however, is inconsistent with recent proxy observations of monsoonal precipitation in Northwest Australia (Zhang et al., 2020; 2022) and previous understanding of EAWM dynamics (Ding et al., 2002; Sun et al., 2006).

We have generated continuous, high-resolution (1 measurement every 0.5 or 1 cm) proxy records of Northwest Australian dust fluxes based on scanning X-ray fluorescence (XRF) and environmental magnetism from IODP Site U1464 (Australian NWS) spanning the last 2.9 Myr. The records show cyclic variability between 2.9 and 1.6 Ma, followed by a marked transition to weak geochemical and magnetic signals in the mid-late Pleistocene. We therefore focus on the 2.9-1.6 Ma time interval. This period corresponds to the initial growth and widespread expansion of continental ice sheets across the Northern Hemisphere mid-high latitudes, expansion of Antarctic ice sheets and sea ice, a strengthening in latitudinal (pole-equator) temperature gradients, and consequent strengthening/repositioning of wind bands. Nonetheless, this time interval pre-dates the Mid-Pleistocene Transition (MPT), when the amplitude of glacial-interglacial cycles and attendant ice-climate feedbacks increased. Thus, our records capture dust-flux variability in the Australian monsoon region in detail over multiple orbital cycles during a time of gradual global climate change, prior to the onset of strong ice-climate feedbacks which have been shown to interfere with insolation/orbital forcing of monsoon and dust flux variability.

In this paper, we describe materials and methods, and then present a new, orbitally-tuned chronology for IODP Site U1464. Accurate dating of sediment sequences from the Australian NWS over the Plio-Pleistocene has proven to be problematic, due to biostratigraphic diachroneity (Groeneveld et al., 2021), magnetostratigraphic ambiguity (Gallagher et al., 2017a; 2017b), and a lack of robust oxygen isotope stratigraphy (Groeneveld et al., 2021). Nonetheless, recent studies have established a revised chronological framework for nearby ODP Site 762 and IODP Site U1463 by combining orbital tuning with biostratigraphic age constraints (Auer et al., 2020; Groeneveld et al., 2021). While these studies incorporated the tuning of benthic $\delta^{13}C$ and/or $\delta^{18}O$ records, we use the strong eccentricity and obliquity signals in our $CaCO_3$ % and Log(Zr/Rb) records for tuning. Finally, we explore the causes of the orbital variability at Site U1464 in the $CaCO_3$ % and dust-flux proxy records.

2. Materials and Methods

2.1. Site Location & Sampling

We use marine cores from IODP Site U1464 (18°03.9′S 118°37.9′E, 264 m water depth, Figure 1), which was cored during IODP Expedition 356 (Gallagher et al., 2017a). This site is located on the central Australian NWS at the southern edge of the modern Australian monsoon region (Figure 1), and lies in the main pathway of aeolian dust fluxes from Northwest Australia that are transported by southeasterly trade winds (Bowler, 1976; Gallagher & deMenocal, 2019) (Figure S1). Site U1464 is thus ideally located to study aeolian flux from Northwest Australia over orbital timescales. A suite of 80 u-channels (each measuring 150 x 2 x 2 cm) were sampled at Kochi Core Center, Japan, in January 2019, from continuous core sections spanning the upper 108.2 m of Hole U1464D. After non-destructive analyses (see below), the u-channels were sub-sampled every 1 cm downcore into ‘cube’ sub-samples of ~4 cm^3 (1 x 2 x 2 cm) for further analyses.

2.2. Scanning X-ray fluorescence (XRF)

All of the Site U1464 u-channels were scanned at 0.5-cm intervals at the Research School of Earth Sciences (RSES), Australian National University (ANU), Canberra, using a third generation Avaatech XRF core scanner. Each u-channel was covered with 4 mm-thick Ultralene film prior to measurement, and then measured at 10 kV with a 0.5 mA current and no filter, 30 kV with a 0.5 mA current and Pd-thin filter, and 50 kV with a 0.6 mA current and Cu filter. Count times of 30 s, 20 s and 10 s were used for these three runs, respectively, and three replicate measurements were taken every 75 cm to check reproducibility. Element spectra were processed into element counts using WinAxil software, and reliable element data were obtained for Ca, Sr, Fe, Ti, Zr, Rb and Si. 141 replicate samples are measured three times for estimation of uncertainties, and precision for Ca, Sr, Fe, Ti, Zr, Rb and Si counts in studied interval was 0.2 %, 0.4 %, 0.7 %, 4.7 %, 3.3 %, 10.2 % and 1.0 %, respectively.

2.3. XRF Calibration

To convert the scanning XRF 'counts' into element concentrations, 50 of the cube subsamples were chosen to cover a range of lithologies (based on the XRF scan results) and depth intervals. Approximately ~0.2 g of each cube sample was oven-dried and ground with an agate mortar and pestle. Sediment powder samples were soaked and extracted using 2 mL nitric acid and 1 mL hydrochloric acid, and the supernate was diluted for the measurement. Single element concentrations were determined using an Inductively Coupled Plasma Optical Emission Spectrometer (ICP-OES) 5110 by Agilent at the RSES, ANU. High quality control of the ICP-OES measurements was based on 10 certified reference materials (marine sediments BCSS-1, MESS-1 and estuarine sediments 1646). Ca, Sr, Fe and Ti concentrations were well-above detection limits for this method, with measurement precisions of 3.616 ‰, 0.007 ‰, 2.154 ‰ and 0.010 ‰, respectively (Table S1).

The Ca, Sr, Ti and Fe ICP-OES concentrations were used to convert Ca, Sr, Ti and Fe XRF counts into concentrations using a multivariate log-ratio calibration, following Weltje et al. (2015). This calibration method is more reliable than a basic univariate calibration (i.e., that based on element-by-element regressions), which does not account for physical constraints on compositional data or matrix effects due to the presence of other elements (Weltje et al., 2015). An undefined variable is included in our calibration and is here termed 'everything else', hence the relative concentrations of elements Ca, Sr, Ti, Fe and 'everything else' sum to 100%. The predictive power of our calibration has been assessed by cross-plotting the reference with the predicted concentrations (Figure S2). High r^2 values for Sr, Ti and Fe indicate a robust calibration, which is strongest for Fe (0.92) and Sr (0.91). Nonetheless, due to calibration problems for high carbonate material (Ellis et al., 2019), the relatively low r^2 value for Ca suggests that the Ca calibration is not reliable. We therefore use the relationship between our ln(Ca/Fe) data and shipboard $CaCO_3$ measurements (r^2=0.90) to convert our scanning XRF ln(Ca/Fe) record into estimated $CaCO_3$ content (Table S2), following Liebrand et al. (2016).

2.4. Environmental magnetism

Magnetic properties were measured on all u-channels at 1-cm intervals using a 2-G Enterprises Model 760 cryogenic magnetometer at the Black Mountain Paleomagnetism Laboratory, ANU. For each u-channel, an anhysteretic remanent magnetization (ARM) was imparted in an alternating field (AF) of 100 mT with a superimposed 0.05 mT bias field and then AF demagnetized in 13 steps from 5 mT to 170 mT. Next, an isothermal remanent magnetization (IRM) was imparted in a 1 T field, which was demagnetized in 13 stepwise AFs from 5 mT to 170 mT. The first/last four measurements of each parameter for every u-channel (topmost and lowest 4 cm) were discarded to avoid edge effects impacting the resultant ARM and IRM records.

2.5. Spectral analysis

To investigate the cyclicity of our time-series, power spectra were obtained using the REDFIT 3.8c (Schulz & Mudelsee, 2002) and cross-checked by the Multitaper method (Thomson, 1982). Data were binned (averages in contiguous 0.3 kyr segments) to retain as much information as possible, while avoiding the introduction of spurious serial dependence. Additionally, the cross wavelet algorithm of Grinsted et al., 2004 was employed to investigate the phase relationship and time evolution of specific cycles (records were resampled to 1 kyr bins before wavelet analysis).

3. Chronology

3.1. Bayesian age-depth model based on biostratigraphic ages

An initial chronology was developed for the upper ~126 m of IODP Site U1464 based on shipboard biostratigraphy. For this, nineteen age control-points (Table S3) were used to construct a Bayesian age-depth model using the "Bacon" package (Blaauw & Christen, 2011) (Figure 2a). Cumulative depths below seafloor (CSF-A) for holes U1464B and U1464D were converted to composite splice depths (CCSF-A) before modeling, based on the established linear relationship between CSF-A and CCSF-A (Gallagher et al., 2017a), and a lithologic boundary was imposed in the model at 43 m CSF-A (= 44.87 m CCSF-A), based on the Unit II/I transition in hole U1464D (Gallagher et al., 2017a). Age uncertainties of the U1464 biostratigraphic datums are mainly from Backman et al. (2012), Wade et al. (2011) and Gallagher et al. (2017a), and all dates are close to or within the 99% probability interval of our Bacon age-depth model. The last occurrence of *G. ruber* (pink) given by Thompson et al. (1979) is also consistent with our age model (Figure 2a).

3.2. Refined age-depth model based on orbital tunings

Additional age control over the interval below ~47 m CSF-A was then investigated using our scanning XRF records, with the goal of orbital tuning (geochemical signals are too weak/ambiguous in the upper ~47 m at this site). Log(Fe/Ca) has been used as a riverine proxy and a tuning target in marine sediments offshore Northwest Australia, while Zr/element ratios have been used as dust proxies (Stuut et al., 2014, 2019; Pei et al., 2021). However, Log(Fe/Ca) at Site U1464 (and other terrigenous element concentrations) appears to primarily reflect $CaCO_3$ variations (Figure 3; see also Section 4.1). Power spectra of our $CaCO_3$, Log(Zr/Fe) and Log(Zr/Rb) records reveal significant cyclicity at ~413 kyr (long eccentricity) for $CaCO_3$ based on depth scale and our biostratigraphic Bayesian model, and at ~41 kyr (obliquity) for Log(Zr/Fe) and Log(Zr/Rb) based on our eccentricity tuning model (Figure S3; Figure S4). Therefore, we focus first on tuning Site U1464 $CaCO_3$, (Section 3.2.1), followed by further fine-tuning (to improve age control) using Log(Zr/Rb) (Section 3.2.2). Finally, we re-ran the Bacon age model using all age constraints with their uncertainties (Section 3.3), thus yielding a new orbitally-constrained, statistically evaluated chronology for Site U1464.

3.2.1. $CaCO_3$ tuning at eccentricity 400 kyr band

Spectral analyses revealed significant power in Site U1464 $CaCO_3$ at frequencies of ~0.0024 kyr^{-1}, equivalent to 413 kyr periodicity (Figure S3a, S3f; Figure S4). This periodicity has previously been used as a tuning target for paleoclimate records from the adjacent IODP Site U1463 (Figure 1) (Christensen et al., 2017; De Vleeschouwer et al., 2018; Groeneveld et al., 2021). $CaCO_3$ content in marine sediments is mainly driven by carbonate production and water column/seafloor dissolution (Keil et al., 2017), and its long-term variations have been shown to be paced by Earth's ~400 kyr eccentricity cycle (Kochhann et al., 2016; Liebrand et al., 2016; Moore et al., 1982). The possible mechanism for ~400 kyr eccentricity cyclicity in $CaCO_3$ at Site U1464 is outlined in Section 4.1. Comparison of Site U1464 $CaCO_3$ with eccentricity shows that $CaCO_3$ maxima tend to correspond with (413 kyr) eccentricity minima (Figure 4), which is consistent with a negative correlation between insolation minima and enhanced sedimentary carbonate content in previous studies, and *vice versa* (Kochhann et al., 2016; Liebrand et al., 2016). This anti-phasing has also been observed in the benthic and planktonic foraminiferal $\delta^{13}C$ records of nearby IODP Site U1463 (De Vleeschouwer et al., 2018; Groeneveld et al., 2021), as well as in global-scale benthic and planktonic $\delta^{13}C$ records (Kochhann et al., 2016; Liebrand et al., 2016; Pälike et al., 2006; Turner et al., 2014; Wang et al., 2010), and likely indicates a ~400 kyr rhythm in the oceanic carbon reservoir. Additional graphic evidence for anti-phasing between Site U1464 $CaCO_3$ and eccentricity is the cycle-shape of $CaCO_3$ variations, which display broad troughs and narrow peaks, i.e., pacing with the inverse of the 413 kyr eccentricity cycle (Figure 4). The Site U1464 chronology was therefore further constrained by four tie-points between eccentricity minima and $CaCO_3$ maxima, after trialing different tuning options (Figure S5; Table S4; Supporting Information Text S1). The tie-points all fall within the 99% confidence intervals of the Bacon age-depth model, hence they are consistent with the Site U1464 biostratigraphy (Figure 2a).

3.2.2. Log(Zr/Rb) tuning at obliquity 41 kyr band

Spectral analyses of the rescaled records after eccentricity tuning revealed significant power in Log(Zr/Rb) (and Log(Zr/Fe) and $IRM_{1T@AF\ 170mT}$) at ~0.024 kyr^{-1} (equivalent to ~41 kyr periodicity, Figure S3). Several studies have used Zr as a dust proxy in sediments offshore Northwest Australia (Pei et al., 2021; Stuut et al., 2014, 2019), as windblown heavy/coarse minerals (e.g., $ZrSiO_4$) are enriched in Zr. Conversely, Rb and Fe are preferentially incorporated into riverine fine-grained clays (Pei et al., 2021; Rothwell & Croudace, 2015; Stuut et al., 2014, 2019), and thus Log(Zr/Rb) and Log (Zr/Fe) likely reflect aeolian/fluvial (or aeolian) fluxes (see Section 4.2 for further discussion). Bandpass filtering of Log(Zr/Rb) at 0.023-0.027 kyr^{-1} frequencies reveals close (positive) covariation with obliquity (Figure 5). Recent studies observed an inverse relationship between Australian summer monsoon precipitation proxies (local surface seawater $\delta^{18}O$ and ln(K/Ca) at IODP Site U1483) and obliquity during the Late-Pleistocene (Zhang et al., 2020; 2022), where higher obliquity was associated with less precipitation (hence less vegetation cover and more erodible particles) and *vice versa*. Similarly, a model-based investigation of obliquity forcing suggested stronger southeasterly trade winds during higher obliquity (Bosmans et al., 2015); such a scenario would favour transport of dust particles from Northwest Australia to Site U1464. Based on this obliquity-dust relationship and the close match of obliquity with our filtered Log(Zr/Rb) record, we further constrain our Site

U1464 chronology with 32 additional tie-points between minima in obliquity and our filtered Log(Zr/Rb) record (Figure 5; Table S5; Figure 2a).

3.3. Refined Bayesian chronology based on biostratigraphy and orbital tunings

To consider potential uncertainties of all age constraints, we re-ran the Bacon age model using the 55 age controls, including 17 biostratigraphic ages, 4 eccentricity tuning ties, 32 obliquity tuning ties, the last occurrence of *G. ruber* (pink) and modern age at the seafloor. This refined Bacon age model can account for most of the age constraints within its 99.99% confidence interval, with the exception of four biostratigraphic datums which are clearly outside the model (Figure 2b).

Comparison of our Site U1464 chronology with recent chronostratigraphic studies of NWS sediments reveals some inconsistencies. For example, dynamical time warping was employed to align a portion of the Site U1464 wireline natural gamma ray (NGR) record (on depth) to that of neighboring Site U1463 (Groeneveld et al., 2021). Conversion of the dynamically warped U1464 depths to CCSF depths and to our age-scale reveals that five (two) points lie outside (inside) our 99% confidence intervals (green crosses in Figure S6). Another offset occurs between some re-dated NWS biostratigraphic datums (based on a revised chronostratigraphy for Site U1463; Groeneveld et al., 2021) and the shipboard ages for these datums at Site U1464 (purple crosses on Figure S6). It is difficult to ascertain which chronostratigraphic markers are more/less reliable, especially as dating NWS sediments from IODP Expedition 356 has not been straightforward (Gallagher et al., 2017a; Groeneveld et al., 2021). There appears to be diachroneity among many biostratographic datums (Gallagher et al., 2017a; Groeneveld et al., 2021), magnetic intensities (for magnetostratigraphy) are weak (Gallagher et al., 2017a, 2017b), and $\delta^{18}O$ stratigraphy is either absent or presents a noisier signal compared to deeper ocean sites (Groeneveld et al., 2021; Pei et al., 2021; Stuut et al., 2014, 2019). In addition, wireline logs and scanning XRF records from upper Pleistocene sediments at Site U1463 and U1464 show weak signals (Gallagher et al., 2017a, 2017b; Groeneveld et al., 2021; this study). This may account for uncertainties in dynamic warping between Sites U1463 and U1464, such as observed in Figure S6. However, while our inferred U1464 ages may be up to 200 kyr older at ~60-90 m and ~130 m, shifting our age-depth relationship in that direction would be at odds with the majority of the biostratigraphic datums, as well as with the eccentricity tuning. For the latter, we tried 12 different tunings (Figure S5; Table S4; Supporting Information Text S1), but all alternatives result in too much stretching/squeezing (hence unrealistic sedimentation rates and changes) or inconsistent eccentricity-$CaCO_3$ relationships (Figure S5). Therefore, in light of our (generally) compatible Bayesian model with biostratigraphy and orbital tunings, we consider our chronology to be sufficiently robust for Site U1464, bearing in mind the aforementioned caveats.

4. Results and Discussion

4.1. Carbonate variations at IODP Site U1464

The calibrated scanning XRF results show that $CaCO_3$ and Sr have consistent variations (Figure 3), indicative of their marine/biogenic origins (Rothwell & Croudace, 2015). Fe, Ti, Rb and Zr also show similar trends (Figure 3), which likely indicate terrigenous signals as these are typical detrital elements (Rothwell & Croudace, 2015). However, marine and terrigenous variations have an inverse relationship, hence their co-variability may be driven by marine carbonate production, carbonate dissolution, or dilution by terrigenous inputs. Calculated total mass accumulation rates (MARs) appear to be more consistent with $CaCO_3$ and Sr MARs variations compared to terrigenous element MARs (Figure S7), which suggests that carbonate production/dissolution, rather than terrigenous dilution, predominated in bulk sediment geochemical variations at Site U1464 between ~2.9 and ~1.5 Ma. This inference is consistent with low Al and K concentrations in ICP-OES and scanning-XRF results from Site U1464, which reflect a minor clay mineral-bound fine-grained fraction of riverine runoff on the Australian NWS (Kuhnt et al., 2015; Rothwell & Croudace, 2015; Zhang et al., 2020). Our inference is further supported by the distinct 413 kyr eccentricity signal in Site U1464 $CaCO_3$ and a known ~400 kyr rhythm in the oceanic carbon reservoir (Kochhann et al., 2016; Liebrand et al., 2016; Pälike et al., 2006; Wang et al., 2010). Additionally, the significant 413 kyr signal in Site U1464 $CaCO_3$ may be attributed to ~2.4-Myr amplitude modulation (AM) (Liebrand et al., 2016), as our study interval falls within the last 2.4-Myr eccentricity minimum (Figure 4); i.e., there is relatively more power in the 400 kyr eccentricity cycle during minima in the 2.4-Myr eccentricity cycle (Laskar et al., 2004).

Calcification rates for $CaCO_3$ shell-forming organisms are closely linked to the $CaCO_3$ saturation state (Ω), which is expressed as: $[\mathrm{Ca}^{2+}][\mathrm{CO}_3^{2-}]/\mathrm{K}_{\mathrm{sp}}^{*}$, where K_{sp}^{*} is the stoichiometric solubility product for $CaCO_3$ (Feely et al., 2004; Kleypas et al., 1999). Ω depends mainly on the concentration of $[CO_3^{2-}]$, since the seawater Ca^{2+} concentration is relatively stable over the studied timescale. Natural and culture experiments indicate that most calcifying organisms, especially those with aragonite or high-Mg calcite, may decrease carbonate production in response to a decreased $[CO_3^{2-}]$, even for $\Omega > 1$ (Beaufort et al., 2011; Feely et al., 2004; Kleypas et al., 1999). In addition, decreased $[CO_3^{2-}]$ and saturation state could reduce abiotic carbonate precipitation on the NWS (Gallagher et al., 2018; Hallenberger et al., 2019; 2022). $CaCO_3$ dissolution is unlikely to have occurred at Site U1464 due to its relatively shallow water-depth compared to the lysocline and carbonate compensation depth. $CaCO_3$ variations at Site U1464 are therefore interpreted to mainly reflect changes in local sea-water $[CO_3^{2-}]$ and related $CaCO_3$ production.

Percentage carbonate at Site U1464 was relatively elevated at ~2.89-2.74 Ma, ~2.46-2.34 Ma, ~2.13-1.89 Ma and ~1.71-1.58 Ma (Figure 6). These broad variations are also registered in benthic $\delta^{13}C$ at IODP Site U1482 offshore Northwest Australia and at Deep Sea Drilling Project (DSDP) Site 593 in the southwest Pacific, but less obviously in benthic $\delta^{13}C$ at nearby Site U1463 (Figure 6), although 413 kyr variability has been demonstrated in the latter record over ~5.2-1.7 Ma (Groeneveld et al., 2021). The benthic $\delta^{13}C$ discrepancy between Site U1463 and U1482/593 may be attributed to different benthic foraminifera species. Epifaunal *P. wuellerstorfi* $\delta^{13}C$ (at Site U1482, Chen et al., 2022 and Site 593, McClymont et al., 2016) usually records bottom-water dissolved inorganic carbon $\delta^{13}C$ in a positive relationship, however infaunal *Uvigerina* spp. $\delta^{13}C$ (at Site U1463, Groeneveld et al., 2021) is also influenced by bottom-water dissolved oxygen content and organic matter fluxes to the sea-floor, which can bias its $\delta^{13}C$ toward more negative values (Mackensen & Schmiedl, 2019). We therefore focus on and interpret the positive covariation between Site U1464 $CaCO_3$ and Site U1482/Site 593 $\delta^{13}C$ records, in terms of seawater dissolved inorganic carbon $[CO_3^{2-}]$ and $\delta^{13}C$.

Considering the water masses influencing these records, the seafloor at Site U1464 (~270 m water depth at present) is currently bathed by the Leeuwin Undercurrent (LUC), and its water-masses mainly derive from Sub-Antarctic Mode Water (SAMW) and/or Antarctic Intermediate Water (AAIW) via the Flinders Current offshore South Australia (Herraiz-Borreguero & Rintoul, 2011; Richardson et al., 2019; Wijeratne et al., 2018; Wong, 2005; Woo & Pattiaratchi, 2008). Seawater temperature profiles nearby based on *in-situ* and modeling data also show a cold water-mass at ~150-100 m depth, indicating intrusion of a southerly-sourced cold water mass (Ridgway & Godfrey, 2015). SAMW is characterized by high-oxygen content (Herraiz-Borreguero & Rintoul, 2011; Woo & Pattiaratchi, 2008), while AAIW is characterized by a salinity minimum (Wong, 2005; Woo & Pattiaratchi, 2008) and low-$[CO_3^{2-}]$, thus making it relatively corrosive to carbonate. Profiling float data show that modern SAMW and AAIW are injected northward into the Indian Ocean at ~15°S (Herraiz-Borreguero & Rintoul, 2011; Wong, 2005), and this northward penetration extends to Site U1464. These water masses can be identified in $[CO_3^{2-}]$, oxygen and salinity profiles from the GLODAPv2.2021 dataset for two transects off Western Australia (Figures S8, S9).

P. wuellerstorfi $\delta^{13}C$ at DSDP Site 593 mainly reflects the dissolved inorganic carbon $\delta^{13}C$ of intermediate water, which is primarily southern-sourced AAIW with minor local contributions (Elmore et al., 2015; McClymont et al., 2016). *P. wuellerstorfi* $\delta^{13}C$ at Site U1482 records the dissolved $\delta^{13}C$ content of Indonesian Intermediate Water (IIW), which originates from AAIW in the western Pacific (Figure S8b, c; Figure S9b, c) (Talley & Sprintall, 2005; Zenk et al., 2005; Wong, 2005). Thus, the intrusion intensity of low-$[CO_3^{2-}]$ AAIW to Sites U1464 and DSDP 593, and indirectly to Site U1482, or changes in AAIW $[CO_3^{2-}]$, may explain co-variability in the respective $CaCO_3$ and $\delta^{13}C$ records (Figure 6). In addition, the proximity of Sites U1464 and U1482 suggests a more direct influence of water masses. At Site U1482, dissolved $[CO_3^{2-}]$ is high in surface waters due to photosynthesis and decreases with depth as organic matter degrades (Figure S8a, S9a). Dissolved $\delta^{13}C$ in the water column reflects this biological process, whereby surface/intermediate waters are characterized by heavy/light $\delta^{13}C$, respectively. Indonesian surface waters feed the south-flowing Leeuwin Current which overlies the Australian NWS; hence, the ventilation and mixing of Intermediate and surface waters at Sites U1482 and U1464 could account for similar trends in their respective $\delta^{13}C$ and $CaCO_3$ % records (Figure 6a). This interpretation is in line with hypotheses that ocean circulation played an important role in the ~400 kyr eccentricity forcing of the global oceanic carbon reservoir (e.g., Wang et al., 2010).

4.2. Aeolian inputs to IODP Site U1464

From our scanning XRF results, Zr, Fe and Rb values can be used to isolate the aeolian component from the total terrestrial composition at Site U1464. Log(Zr/Fe) has been used at ODP Site 762 (Figure 1) as a proxy for aeolian dust from Northwest Australia (Stuut et al., 2014, 2019). Log(Zr/Fe) can indicate the transport pathway and grain-size of terrigenous particles, since the wind-blown fraction is enriched in Zr due to its presence in coarser and/or heavier grains, whereas Fe is enriched in run-off sediments (Stuut et al., 2014, 2019). We also use Log(Zr/Rb) as a dust proxy, as Rb is preferentially incorporated into riverine fine-grained clays (Pei et al., 2021; Rothwell & Croudace, 2015). The Log(Zr/riverine element) ratio is therefore used to estimate the relative contribution of aeolian versus riverine inputs.

Isothermal remanence magnetism (IRM) has also been used to approximate past aeolian dust fluxes in marine cores (Larrasoaña et al., 2003; Grant et al., 2022), where the IRM remaining after AF demagnetization at 170 mT ($IRM_{1T@AF\ 170mT}$) reflects the relative contribution from magnetic minerals with a coercivity of remanence larger than 170 mT (i.e., imperfect antiferromagnetic minerals, such as hematite) (Verosub & Roberts, 1995). Hematite is generally thought to be preferentially formed in dry and hot environments, and then transported to marine sediments via aeolian dust. Because hematite concentration is affected by variations in the concentrations of other constituents, the variations of $IRM_{1T@AF\ 170mT}$ may simply reflect dilution by carbonate. To eliminate this dilution effect, $CaCO_3$-free $IRM_{1T@AF\ 170mT}$ was calculated based on the following formula: $CaCO_3$-free $IRM_{1T@AF\ 170mT} = [IRM_{1T@AF\ 170mT}] / (1-[CaCO_3])$, where $[CaCO_3]$ ranges from 0 to 1. The long-term consistency of magnetic susceptibility, ARM, IRM_{1000mT}, $IRM_{1T@AF170mT}$ with $CaCO_3$-free $IRM_{1T@AF\ 170mT}$ indicates that their variations represent the changes in magnetic mineral concentrations, despite some differences in short-term variations (Figure S10), however it is not straightforward to use the magnetic susceptibility, ARM, IRM_{1000mT} as aeolian dust proxies. Thus, we omit to use these magnetic parameters in this study. Broadly consistent long-term trends and higher frequency co-variability in the obliquity band between our magnetic hematite proxy and geochemical dust proxies (Figure 7a-c, Figure S11, note reversed y-axes; see Supporting Information Text S2) corroborate their interpretation as aeolian dust proxies at Site U1464.

For comparison, a Log(Zr/Fe) record is available for ODP Site 762 offshore Northwest Australia (Stuut et al., 2019) (Figure 1; Figures 7e). In terms of absolute values, Log(Zr/Fe) at Site U1464 has higher values than that at ODP Site 762 during the same period. Discrete samples from modern river beds and dune sediments of Northwest Australia showed that Log(Zr/Fe) values of dune sediments are generally greater than -1, while those in river beds are typically less than -1 (Stuut et al., 2019). If modern end-member values are applicable over the Late Pliocene/Early

Pleistocene, it implies that Site U1464 Log(Zr/Fe) values mostly reflect dune end-members (based on a 21-point running average (Figure 7c), although some individual data-points are less than -1), while ODP Site 762 Log(Zr/Fe) values reflect riverine sources (Figure 7e). At first glance this observation appears counter-intuitive, as Site 762 is located further offshore than Site U1464 (Figure S1) and the proportion of riverine (aeolian) components in off-shore sediment tends to decrease (increase) with distance from river mouths (Stuut et al., 2019). However, ODP Site 762 is more proximal to outflow from the Fortescue, Ashburton and Lyndon-minilya rivers than Site U1464 (Figure S1), which, in contrast, lies directly in the path of the Northwest Australian dust belt (Figure S1, Bowler, 1976). An additional/alternative explanation is that Site U1464 lies on the shelf slope at ~260 m water depth, while ODP Site 762 is further offshore at 1360 m water depth, so prevailing currents and sediment dynamics/transport differ between the sites. Inconsistent trends between Site U1464 and Site 762 Log(Zr/Fe) records may therefore be explained by their contrasting locations and associated differences in the proportion of riverine/dust components reaching each site. Chronological offsets/uncertainties could also explain some discrepancies between the records, although it is hard to explain such differing trends by chronology alone (e.g., the records are almost anti-phased between ~2.9 and ~2.4 Ma).

Better agreement is observed between our IODP Site U1464 Log(Zr/Fe) record and a downhole natural gamma radiation (NGR)-derived Th/K record from neighboring IODP Site U1463 (Christensen et al., 2017) (Figure 1; Figure 7d), taking into account the chronological uncertainties/offsets between these sites. The Th/K record has been interpreted as a dust proxy (Christensen et al., 2017), and potentially synchronous dust maxima can be identified between our dust records and the Site U1463 Th/K record (dashed lines in Figure 7a-d). Nonetheless, there are uncertainties in NGR-derived K and Th measurements (De Vleeschouwer et al., 2017). One limitation is that the wireline NGR system integrates counts from a 40-cm long core, which causes significant smoothing of signals during measurements. Also, the algorithm that produces accurate estimates of K and Th content relies on different density measurements (gamma ray attenuation, moisture and density), and these density measurements can contribute additional errors to the K and Th estimates. The above uncertainties may explain some of the offsets between our U1464 dust proxy records and the Site U1463 Th/K record.

4.3. Obliquity-paced Northwest Australian dust fluxes

Spectral analyses of our dust records reveal significant peaks corresponding to three obliquity frequencies (at ~0.024 kyr^{-1} (41 kyr), ~0.034 kyr^{-1} (29 kyr) and ~0.019 kyr^{-1} (54 kyr), based on Hinnov (2000) and Mélice et al. (2001)) using the Redfit method (Figure S3c-e). These three frequencies are also observed in the Multitaper method (Figure S3h-j), showing that these three obliquity frequencies can be identified using different approaches. Furthermore, the position and relative amplitude of the 0.019 kyr^{-1} peak, and to a lesser extent the 0.034 kyr^{-1} peak, are relatively insensitive to our obliquity tuning and Bacon age modelling (Figure S3; Figure S12), thus underscoring the reliability of our spectral analyses and the dominance of obliquity in Site U1464 dust-flux proxy records. Spectral power in the precession band is less pronounced, and limited to ~19 kyr periodicity (Figure S3). Interestingly, the 0.019 and/or 0.034 kyr^{-1} frequencies have also been detected in Australian monsoon records (Holbourn et al., 2005; Kershaw et al., 2003; Liu et al., 2015; Zhang et al., 2020, 2022) and in aeolian grain size records from other Indo-Pacific regions (Clemens & Prell, 1990; Hovan et al., 1991; Pisias & Rea, 1988), which suggests that these frequencies may be a consistent feature of large-scale atmospheric circulations over the Plio-Pleistocene (see Section 4.4 below).

The spectral peak in Site U1464 dust proxies at ~41 kyr could be explained by a linear response to obliquity forcing, since this is the dominant frequency of obliquity. However, the amplitude of the ~54 kyr peak in our dust proxies is much higher than that of the 41 kyr peak, contrary to the obliquity spectrum (Hinnov, 2000; Laskar et al., 2004; Mélice et al., 2001); the 54 kyr peak may therefore reflect a non-linear response to obliquity forcing or a heterodyne of other orbital frequencies. To investigate the evolution of these two obliquity periods (~0.024 kyr^{-1} and ~0.019 kyr^{-1}) in our time-series, we calculated bandpass-filters of 0.023-0.027 kyr^{-1} and 0.017-0.021 kyr^{-1} in Log(Zr/Rb), and found that the 0.024 kyr^{-1} frequency dominated during the ~2.9-2.24 Ma interval, while the 0.019 kyr^{-1} frequency became dominant after ~2.1 Ma (Figure S13b, c). This frequency shift from 0.024 to 0.019 kyr^{-1} might be attributed to ~1.2-Ma obliquity AM, which decreased during the interval of 2.24-2.1 Ma (Figure S13a) (Hinnov, 2000; Laskar et al., 2004). The transformation from AM into frequency modulation (FM) seems consistent with previously proposed FM hypotheses, in which a high-frequency carrier can be modulated by a low-frequency modulator to create sidebands based on $F_{Carrier} \pm F_{Modulator} = F_{Sideband}$ (Rial, 1999; Rial & Anaclerio, 2000). In this case, the 0.019 (1/54) kyr^{-1} peak in our observation coincides with the sideband of a 0.024 (1/41) kyr^{-1} carrier modulated by a 0.005 (1/171) kyr^{-1} modulator; that is 0.024 - 0.005 = 0.019, in which the ~0.005 (1/171) kyr^{-1} originates from the obliquity AM (Hinnov, 2000; Mélice et al., 2001). Similarly, the 0.034 (1/29) kyr^{-1} peak may also be the sideband of a 0.024 (1/41) kyr^{-1} modulated by the 0.005 (1/171) kyr^{-1} (i.e., 0.024 + 2*0.005 = 0.034). The specific origins of these obliquity signals will be further discussed in the following section.

4.4. Origin of obliquity signals in Northwest Australian dust records

Here we explore possible origins of the dominant obliquity-scale variability in our dust proxy records, and what this reveals about climate forcing of Australian dust fluxes over longer orbital timescales. Two key climate forcings to consider are i) high-latitude climate forcing via ice-sheet fluctuations and/or the EAWM, and ii) direct low-latitude insolation forcing via the SITIG (summer inter-tropical insolation gradient). Both of these mechanisms show strong obliquity periodicities and have been proposed to explain the presence of obliquity cycles in low-latitude monsoon and aeolian dust fluxes (Beck et al., 2018; Ding et al., 2002; Hennekam et al., 2022; Leuschner & Sirocko, 2003; Liu et al., 2015; Stuut et al., 2019; Sun et al., 2006).

4.4.1. High-latitude climate forcing: Glacial cycles and the EAWM

We first note that it is difficult to disentangle the potential influences of glacial cycles and the EAWM, because intensity variations in the EAWM over orbital timescales were closely associated with (Northern Hemisphere) ice-sheet fluctuations (Ding et al., 2002; Sun et al., 2006). Nonetheless, ice sheets and EAWM intensity could affect Northwest Australian dust fluxes by different mechanisms. For example, the extent of large Northern Hemisphere ice sheets determines pole-equator temperature gradients and the position and strength of latitudinal wind bands (Clark et al., 1999; Ganopolski et al., 1998), and we could consider this as an 'indirect' forcing of Northwest Australian dust fluxes, as it pertains to global atmospheric changes. Additionally, Northern Hemisphere ice sheets could indirectly influence NWS dust variations via sea-level fluctuations, as the distance between coastline and Site U1464 might control fluvial inputs (Stuut et al., 2019) and consequently influence dust content via fluvial dilution. In contrast, the EAWM is directly coupled to the Australian monsoon via cross-equatorial flows (Liu et al., 2015; Suppiah, 1992; Suppiah & Wu, 1998). Accordingly, past changes in Northwest Australian dust fluxes may have been influenced indirectly by ice-sheet forcing via large-scale atmospheric circulations and sea-level fluctuations, or directly by EAWM intensity via local cross-equatorial flows.

We compare our dust records to global sea level (= ice volume) and to a stacked mean grain-size of quartz (MGSQ) record from the Chinese Loess Plateau (Figure 8a-d), to investigate whether the obliquity signal in the Site U1464 dust fluxes reflects an indirect influence of Northern Hemisphere ice sheets or a direct influence of EAWM intensity. Clearly, our Australian dust-flux reconstructions show no consistent phasing with ice volume, even if both have high common power at the 41 kyr obliquity band (Figure 8a, b; Figure S12a). In addition, our geochemical results show that terrestrial sediments are mainly composed of aeolian dust at Site U1464 and indicate that fluvial input was minor. The palaeodepth estimation (>300 m water depth during the Early Pleistocene) (Gallagher et al., 2017a) and absence of potential river sources at Site U1464 further suggest that this region was unlikely to receive significant amounts of fluvial siliciclastic input. Accordingly, the 41 kyr cycles in our dust proxies were unlikely influenced by fluvial dilution caused by eustatic sea-level fluctuations. From these observations, we can rule out the 'indirect' forcing of ice volume, consistent with previous studies about the Indian summer monsoon based on Arabian Sea sediments (Clemens et al., 1991a; Clemens & Prell, 2003; Leuschner & Sirocko, 2003) and the (Early Pleistocene) North African monsoon based on eastern Mediterranean Sea sediments (Hennekam et al., 2022; Reichart, 1997). Although there is no linear correlation between global ice volume and Northwest Australian dust fluxes, ice volume might exert an influence indirectly via the EAWM, given that the EAWM was influenced by North Hemisphere ice sheets (Ding et al., 2002; Sun et al., 2006).

Comparison between Site U1464 Log(Zr/Fe) and the stacked MGSQ record reveals that Northwest Australian dust flux had a similar, but anti-phased, long-term trend with EAWM intensity (Figure 8c). In general, decreased dust fluxes off Northwest Australia correspond to a stronger EAWM, and *vice versa*. A straightforward explanation is that enhanced (diminished) EAWM intensity would favor a stronger (weaker) Australian summer monsoon, expanded (reduced) vegetation cover, less (more) erodible particles in source areas, and dampening (strengthening) of southeast trade winds which transport dust from the Australian interior towards the NWS. Three peaks associated with obliquity frequencies are present in both records over the 1.6-2.9 Ma interval (Figure S12b, d-f); however, cross-wavelet analysis suggests an ambiguous relationship between Site U1464 dust fluxes and EAWM variability at obliquity frequencies (Figure 8d). This inconsistency may be an artifact of age model uncertainties and assumptions in both records. For example, different obliquity phasings were assumed in their orbital tuning. The stacked MGSQ chronology involves an assumed 8-kyr lag with respect to obliquity (Ding et al., 2002; Sun et al., 2006), while we assumed zero phase lag between Site U1464 dust fluxes and obliquity in this study. We did, however, apply an age uncertainty of ±20-kyr for the obliquity tuning tie-points in our Bacon age model. The 8-kyr lag for the MGSQ record is based on SPECMAP (Imbrie et al., 1984); hence, it is based on relatively large amplitude glacial-interglacial cycles of the Late Pleistocene, whereas a smaller lag should be expected for the Early Pleistocene. Equally, there may be an ice-volume effect on our dust records, via the EAWM, in which case a lagged obliquity tuning may be more appropriate. Therefore, although we cannot objectively compare obliquity-band phasing of our dust records with the stacked MGSQ record, we nonetheless propose EAWM intensity as a possible origin of the obliquity cycles observed in our Site U1464 dust-flux time series, given the similarity of their long-term trends and obliquity-band spectral peaks, and a known physical mechanism (cross-equatorial flow) linking the two monsoon regions.

4.4.2. Low-latitude SITIG forcing

The SITIG (i.e., the difference in summer insolation between 30° N and 30° S) is a low-latitude insolation forcing which contains notable precession and obliquity components (unlike, for example, 30° N or 30° S insolation time-series), and has been invoked as a potential driver of East Asian (Beck et al., 2018), Indian (Leuschner & Sirocko, 2003) and African monsoon (Reichart, 1997) variability over orbital timescales. This monsoon-forcing mechanism has been corroborated by model simulations and has a physical basis as described by previous studies (Beck et al., 2018; Bosmans et al., 2015; Mantsis et al., 2014). In this mechanism, a stronger SITIG can drive an intensified winter Hadley circulation and thus a stronger cross-equatorial moisture transport into the summer hemisphere, and this has been validated for seasonal (Schwendike et al., 2014) and orbital timescales (Beck et al., 2018; Bosmans et al., 2015; Mantsis et al., 2014).

Obliquity plays a key role in modulating the SITIG and meridional heating gradients. Several modelling studies have demonstrated that when the SITIG is stronger during higher obliquity, high-pressure anticyclones in the Southern Hemisphere (which form the descending limb of the winter hemisphere Hadley cell) are strengthened, while high-pressure anticyclones in the Northern Hemisphere (which form the descending limb of the summer hemisphere Hadley cell) are weakened (Beck et al., 2018; Bosmans et al., 2015; Mantsis et al., 2014; Schwendike et al., 2014). Thus, during a stronger obliquity-induced SITIG, intensified cross-equatorial winds and moisture transport into the Northern Hemisphere is consistent with intensified southeasterly trade winds and a more arid Australian interior, and *vice versa*. Northwest Australian dust fluxes can therefore respond immediately to changes in the SITIG via these dynamics. Since muted precession and large obliquity are present in Site U1464 dust proxy records (Figure S3), the summer half-year (21 March - 20 September), instead of one single month, was calculated in the SITIG as follows: SITIG = $I_{March\text{-}September}$ (30° N) - $I_{March\text{-}September}$ (30° S), where $I_{March\text{-}September}$ (30° N or 30° S) is sum of monthly insolation from 21 March to 20 September at 30° N or 30° S. This calculation can amplify obliquity and mute precession (Figure S12c), and is hence more consistent with our observations. There is reasonable agreement between Site U1464 dust fluxes and SITIG before 2.55 Ma and after 2.35 Ma (Figure 8e, f), in both frequency and amplitude variability. Between 2.55 and 2.35 Ma the records appear to be offset, i.e., there appears to be a phase lag of dust flux relative to the SITIG. Given that we assumed no phase lag in our obliquity tuning (based on the near-direct mapping of the filtered Log(Zr/Rb) onto obliquity prior to tuning, Figure 5), comparison of the SITIG to our dust proxy record cannot include interpretation of phase relationships. Nonetheless, the agreement through most the records in both amplitude and dominant frequency is consistent with SITIG forcing of Northwest Australian dust fluxes through the Early Pleistocene.

An additional/alternative consideration is that the 54 kyr obliquity cycle in our dust records might be amplified by a nonlinear response to the AM of obliquity (and hence to the resultant SITIG). For example, the long-term mean of the SITIG AM narrowed down to a lower value during ~2.24-2.1 Ma due to the 1.2-Myr obliquity AM (Figure S13a), and the decreased amplitude of SITIG variability, amplified by internal climate feedbacks, could have shifted the sensitivity of Northwest Australian dust fluxes to SITIG forcing from a 41 kyr cycle to a prolonged 54 kyr cycle (Figure S13b, c). On one hand, smaller amplitude in the SITIG would reduce the relative strength of winter Hadley circulation and associated cross-equatorial flows between SITIG maxima and minima, thereby weakening the 41 kyr effect on dust fluxes over Northwest Australia. On the other hand, smaller SITIG amplitude after ~2.1 Ma would make the

171 kyr AM cycle comparable or stand out with respective to the 41 kyr cycle, which would explain the presence of 171 kyr cycles in our dust records (Figure S13a, d, e). The 54 kyr spectral peak is dominant over the 41 kyr peak in our dust records, especially after ~2.1 Ma (Figure S13b, c, d, e), and may have been amplified by a FM mechanism based on 0.024 (1/41) - 0.005 (1/171) = 0.019 (1/54) (Rial, 1999; Rial & Anaclerio, 2000).

4.4.3. Insights from other Indo-Pacific dust records

Orbitally-driven changes in the intensity of the EAWM, the SITIG, or both, may underpin the dominant obliquity cycles observed in Site U1464 dust-flux reconstructions. For further insights, we therefore turn to other Indo-Pacific dust records. Interestingly, dust-flux time-series from Site RC27-61 in the northwestern Arabian Sea (Clemens & Prell, 1990; Clemens et al., 1991a), Site RC11-210 in the central Equatorial Pacific (Pisias & Rea, 1988) and Site V21-146 in the Northwest Pacific (Hovan et al., 1991) all contain cycles at 54 and/or 29 kyr, in addition to 41 kyr, similar to our Site U1464 dust records. Australian monsoon records also show these three obliquity cycles (Holbourn et al., 2005; Kershaw et al., 2003; Liu et al., 2015; Zhang et al., 2020, 2022), while these spectral peaks are not present in the sea level time-series spanning this timeframe (Figure S12a). These findings imply that our Site U1464 dust-flux reconstruction likely reflects a component of low-latitude, Indo-Pacific climate variability that is independent of ice-sheet related variability.

The long-term variability of Walker circulation and sea surface temperature (SST) gradients in the tropical Pacific and Indian Ocean (i.e., ENSO-like) might amplify the 29 kyr cycles via resonance with obliquity (Beaufort et al., 2001; Pisias & Rea, 1988). The 29 kyr period was dominant in easterly trade wind intensity and equatorial divergence in the central Equatorial Pacific during the Late Pleistocene, based on aeolian grain-size and relative abundance of two radiolarian species, respectively (Pisias & Rea, 1988). This 29 kyr cycle was also found as a secondary period in: central Equatorial Pacific SST (Pisias & Rea, 1988); southern subtropical Indian Ocean SST (Clemens et al., 1991a, b); wind strength of the southwest monsoon in the northwestern Arabian Sea (Clemens & Prell, 1990; Clemens et al., 1991a, b); and, primary productivity associated with the tropical Indo-Pacific thermocline (Beaufort et al., 2001). This non-primary 29 kyr variability inherent in these records strongly suggests that the resonance between obliquity and tropical Indo-Pacific atmosphere-ocean dynamics may play a key role in amplifying the 29 kyr variability in our dust records.

5. Conclusions

We present $CaCO_3$ and aeolian dust proxy records (Log(Zr/Rb), Log(Zr/Fe) and $CaCO_3$-free $IRM_{1T@AF\ 170mT}$) for IODP Site U1464 on the Northwest Shelf of Australia from the Early Pleistocene (~1.6 - 2.9 Ma). A new, orbitally-tuned chronology was constructed for Site U1464 using a Bayesian model of biostratigraphic datums in conjunction with eccentricity- and obliquity-tuning of our $CaCO_3$ and Log(Zr/Rb) timeseries.

A ~400 kyr (eccentricity) cyclicity is present in the $CaCO_3$ record similar to benthic $\delta^{13}C$ records from the wider region, where the benthic records are typically indicative of intermediate water $\delta^{13}C$, and where $CaCO_3$ and $\delta^{13}C$ minima are associated with maxima in the 400 kyr eccentricity cycle (and *vice versa*). These observations are consistent with a ~400 kyr pacing of the oceanic carbon reservoir via ocean ventilation and large-scale circulation.

Obliquity frequencies dominate the dust proxy records at Site U1464. Three obliquity cycles (41 kyr, 54 kyr and 29 kyr) are present and we explore their possible origins in terms of low- *versus* high-latitude forcing mechanisms. The 41 kyr signal in Northwest Australian dust fluxes may originate from fluctuations in the intensity of the EAWM and/or the SITIG, both of which are directly driven by obliquity variations. In contrast, the 54 kyr signal in the dust-flux records might result from a non-linear response to AM of obliquity and attendant SITIG variability. The resonance between obliquity and tropical Indo-Pacific atmosphere-ocean dynamics may also be an amplifying mechanism of secondary obliquity frequencies, especially for the 29 kyr cycle, which is detected in other paleoclimate proxy records from the Indo-Pacific region.

Figure 1. Precipitation (land), sea surface temperature (SST, ocean) and 850 hPa wind patterns of the Australian-Indonesian region for average austral summer (DJFM, top) and winter (JJAS, bottom). Precipitation data (1901-2013) is from the GPCC dataset (Schneider et al., 2011); SST data (1870-2017) is from the HadISST1 dataset (Rayner et al., 2003); Wind data (1948-2017) is from the NCEP/NCAR Reanalysis (Kalnay et al., 1996). Brown dash lines denote the Pilbara heat low (Suppiah, 1992). Red star marks IODP Site U1464 (this study). Core sites discussed in this study are indicated with black circles: IODP Site U1482 (Chen et al., 2022), IODP Site U1463 (Christensen et al., 2017), ODP Site 762 (Stuut et al., 2019), and DSDP Site 593 (McClymont et al., 2016). Detailed drainage basins (number 1-16) in the black rectangle are shown in Figure S1.

Figure 2. Bacon age-depth models for IODP Site U1464 (red). (a) Bacon age-depth model based on biostratigraphic ages. Black, blue, green, yellow and white dotted lines indicate the model's 99.99%, 99%, 95%, 90% and 80% probability intervals, respectively. (b) Refined Bacon age-depth model based on all biostratigraphic ages and tunings. Gradual darker grey shadings indicate the model's 99.99%, 99%, 95%, 90% and 80% probability intervals, respectively. Red line is the median probability. Red solid circles are biostratigraphic age control-points (Table S3). Blue solid circles are four tie-points between eccentricity and the $CaCO_3$ record (Table S5). Yellow solid circles are 32 tie-points between obliquity and the filtered Log(Zr/Rb) record (Table S5). Black solid circle is the last occurrence of *G. ruber* (pink).

Figure 3. IODP Site U1464 bulk geochemistry from ~1.6 to 2.9 Ma. (a) Log(Fe/Ca); (b) $CaCO_3$; (c) Sr; (d) Fe; (e) Ti; (f) Rb and (g) Zr. Note that (b-e) show calibrated element concentrations, and (f, g) show scanning-XRF element counts. Bold lines (grey lines) in a-g are 21-point running averages (original data).

Figure 4. IODP Site U1464 eccentricity tuning. (a) Site U1464 $CaCO_3$ (gray: original time-series; purple: 21-point running average) on initial Bacon age model. (b) Eccentricity (green, Laskar et al., 2004). (c) Eccentricity (green) and Site U1464 $CaCO_3$ (gray: original time-series; purple: 21-point running average) rescaled after eccentricity tuning. Tie-points are indicated (dotted lines) for visual clarity. Cycle numbers represent 413 kyr eccentricity cycles, counted back from the present. ($CaCO_3$ y-axes are reversed for visual comparison).

Figure 5. IODP Site U1464 obliquity tuning. (a) Site U1464 Log(Zr/Rb) (gray: original time-series; green: 21-point running average) and its 0.023-0.027 band-pass filter (magenta) on the eccentricity tuning age model. (b) Obliquity (black, Laskar et al., 2004). (c) Obliquity (black) and the 0.023-0.027 band-pass filter (magenta) after obliquity tuning. 32 ties between obliquity minima and minima in the 0.023-0.027 filtered Log(Zr/Rb) are indicated (dotted lines) for visualization. Red triangles in (a) represent four eccentricity tuning tie-points.

Figure 6. IODP Site U1464 carbonate content and regional benthic $\delta^{13}C$ records. (a) Site U1464 $CaCO_3$ (purple) and IODP Site U1482 *P. wuellerstorfi* $\delta^{13}C$ (blue, Chen et al., 2022). (b) Site U1464 $CaCO_3$ (purple) and IODP Site U1463 *Uvigerina spp.* $\delta^{13}C$ (green, Groeneveld et al., 2021). (c) Site U1464 $CaCO_3$ (purple) and DSDP Site 593 *P. wuellerstorfi* $\delta^{13}C$ (cyan, McClymont et al., 2016). The eccentricity tuning is used for the age model of Site U1464 $CaCO_3$ to validate the ~400 kyr eccentricity tuning. Red triangles represent four eccentricity tuning tie-points for Site U1464 $CaCO_3$. Blue, green and cyan triangles represent age constraints for Site U1482 *P. wuellerstorfi* $\delta^{13}C$, Site U1463 *Uvigerina spp.* $\delta^{13}C$ and Site 593 *P. wuellerstorfi* $\delta^{13}C$, respectively.

Figure 7. Dust proxy records from the Australian NWS. $CaCO_3$-free $IRM_{1T@AF\ 170mT}$ (a, red), Log(Zr/Rb) (b, green: 21-point running average), and Log(Zr/Fe) (c, blue: 21-point running average) records at Site U1464. Wireline-derived Th/K record at Site U1463 (d, Christensen et al., 2017) and Log(Zr/Fe) record at Site ODP762 on Auer et al. (2020)'s updated age scale (e, orange: 9-point running average, Stuut et al., 2019). Dust maxima events are indicated in dash lines for visual alignment.

Figure 8. Comparison of Northwest Australian dust fluxes with global sea level, EAWM and SITIG from 1.6 to 2.9 Ma. (a) Site U1464 Log(Zr/Rb) and global sea level (Rohling et al., 2021) and (b) their cross wavelet spectrum. (c)

Site U1464 Log(Zr/Rb) and a stacked MGSQ record (Sun et al., 2006) and (d) their cross wavelet spectrum. (e) Site U1464 Log(Zr/Rb) and the SITIG summer half-year (Laskar et al., 2004) and (f) their cross wavelet spectrum. The 30° N-30° S SITIG is shown in e (black) and the 0.023-0.027 filter of Log(Zr/Rb) is also shown in e (red line). In b, d and f, the cone of influence and 5% significance level are indicated by opaque shading and bold black contours, respectively. Arrows pointing to the right indicate an in-phase relationship.

Acknowledgments

This work was supported by the Australian Research Council (ARC) through grant DE1900100042 (K.M.G), the Australia-New Zealand IODP Consortium (ANZIC) Legacy/Special Analytical Funding grant LE160100067 (K.M.G.), the Australian National University-China Scholarship Council (ANU-CSC) Scholarship (S.Z.) and the Shen-su Sun Scholarship (S.Z.). S.G. thanks the USIO staff and the SIEM Offshore crew for their invaluable assistance and skill during IODP Expedition 356 and the Australian IODP office for funding. We thank Andrew P. Roberts and Xiang Zhao for assistance with measurement and analysis of the environmental magnetic data.

Data Availability Statement

Geochemical and environmental magnetic data from IODP Site U1464 were generated in this study. New data are archived in the Zenodo database (Zhao & Grant, 2023).

References

Auer, G., De Vleeschouwer, D., & Christensen, B. A. (2020). Toward a robust Plio-Pleistocene chronostratigraphy for ODP Site 762. *Geophysical Research Letters*, 47(3), e2019GL085198. https://doi.org/10.1029/2019GL085198

Australia's River Basins (1997). Geoscience Australia, Canberra. https://ecat.ga.gov.au/geonetwork/srv/eng/catalog.search#/metadata/42343

Backman, J., Raffi, I., Rio, D., Fornaciari, E., & Pälike, H. (2012). Biozonation and biochronology of Miocene through Pleistocene calcareous nannofossils from low and middle latitudes. *Newsletters on Stratigraphy*, 45(3), 221-244. https://doi.org/10.1127/0078-0421/2012/0022

Baddock, M., Parsons, K., Strong, C., Leys, J., & McTainsh, G. (2015). Drivers of Australian dust: A case study of frontal winds and dust dynamics in the lower Lake Eyre Basin. *Earth Surface Processes and Landforms*, 40(14), 1982-1988. https://doi.org/10.1002/esp.3773

Bayon, G., De Deckker, P., Magee, J. W., Germain, Y., Bermell, S., Tachikawa, K., & Norman, M. D. (2017). Extensive wet episodes in Late Glacial Australia resulting from high-latitude forcings. *Scientific Reports*, 7(1), 1-7. https://doi.org/10.1038/srep44054

Beaufort, L., de Garidel-Thoron, T., Mix, A. C., & Pisias, N. G. (2001). ENSO-like forcing on oceanic primary production during the late Pleistocene. *Science*, 293(5539), 2440-2444. https://doi.org/10.1126/science.293.5539.2440

Beaufort, L., Probert, I., de Garidel-Thoron, T., Bendif, E. M., Ruiz-Pino, D., Metzl, N., et al. (2011). Sensitivity of coccolithophores to carbonate chemistry and ocean acidification. *Nature*, 476(7358), 80-83. https://doi.org/10.1038/nature10295

Blaauw, M., & Christen, J. A. (2011). Flexible paleoclimate age-depth models using an autoregressive gamma process. *Bayesian Analysis*, 6(3), 457-474. https://doi.org/10.1214/11-BA618

Beck, J. W., Zhou, W., Li, C., Wu, Z., White, L., Xian, F., et al. (2018). A 550,000-year record of East Asian monsoon rainfall from ^{10}Be in loess. *Science*, 360(6391), 877-881. https://doi.org/10.1126/science.aam5825

Bosmans, J. H. C., Hilgen, F. J., Tuenter, E., & Lourens, L. J. (2015). Obliquity forcing of low-latitude climate. *Climate of the Past*, 11(10), 1335-1346. https://doi.org/10.5194/cp-11-1335-2015

Bowler, J. M. (1976). Aridity in Australia: age, origins and expression in aeolian landforms and sediments. *Earth-Science Reviews*, 12(2-3), 279-310. https://doi.org/10.1016/0012-8252(76)90008-8

Chappell, J., Syktus, J., Giambelluca, T. W., & Henderson-Sellers, A. (1996). Palaeoclimatic modelling: A western Pacific perspective. In T. W. Giambelluca and A. Henderson-Sellers (Eds.), *Climate Change: Developing Southern Hemisphere Perspectives* (pp. 175-193). John Wiley & Sons.

Chen, Y., Xu, J., Liu, J., Li, T., Xiong, Z., Zhang, P., & Yan, H. (2022). Climatic and tectonic constraints on the Plio–Pleistocene evolution of the Indonesian Throughflow intermediate water recorded by benthic $\delta^{18}O$ from IODP site U1482. *Quaternary Science Reviews*, 295, 107666. https://doi.org/10.1016/j.quascirev.2022.107666

Christensen, B. A., Renema, W., Henderiks, J., De Vleeschouwer, D., Groeneveld, J., Castañeda, I. S., et al. (2017). Indonesian Throughflow drove Australian climate from humid Pliocene to arid Pleistocene. *Geophysical Research Letters*, 44(13), 6914-6925. https://doi.org/10.1002/2017GL072977

Clark, P. U., Alley, R. B., & Pollard, D. (1999). Northern Hemisphere ice-sheet influences on global climate change. *Science*, 286(5442), 1104-1111. https://www.science.org/doi/10.1126/science.286.5442.1104

Clemens, S. C., & Prell, W. L. (1990). Late Pleistocene variability of Arabian Sea summer monsoon winds and continental aridity: Eolian records from the lithogenic component of deep-sea sediments. *Paleoceanography*, 5(2), 109-145. https://doi.org/10.1029/PA005i002p00109

Clemens, S., Prell, W., Murray, D., Shimmield, G., & Weedon, G. (1991a). Forcing mechanisms of the Indian Ocean monsoon. *Nature*, 353(6346), 720-725. https://doi.org/10.1038/353720a0

Clemens, S. C., & Prell, W. L. (1991b). Late Quaternary forcing of Indian Ocean summer-monsoon winds: A comparison of Fourier model and general circulation model results. *Journal of Geophysical Research: Atmospheres*, 96(D12), 22683-22700. https://doi.org/10.1029/91JD02205

Clemens, S. C., & Prell, W. L. (2003). A 350,000 year summer-monsoon multi-proxy stack from the Owen Ridge, Northern Arabian Sea. *Marine Geology*, 201(1-3), 35-51. https://doi.org/10.1016/S0025-3227(03)00207-X

Courtillat, M., Hallenberger, M., Bassetti, M. A., Aubert, D., Jeandel, C., Reuning, L., et al. (2020). New record of dust input and provenance during glacial periods in Western Australia Shelf (IODP expedition 356, Site U1461) from the Middle to Late Pleistocene. *Atmosphere*, 11(11), 1251. https://doi.org/10.3390/atmos11111251

Denniston, R. F., Asmerom, Y., Polyak, V. J., Wanamaker Jr, A. D., Ummenhofer, C. C., Humphreys, W. F., et al. (2017). Decoupling of monsoon activity across the northern and southern Indo-Pacific during the Late Glacial. *Quaternary Science Reviews*, 176, 101-105. https://doi.org/10.1016/j.quascirev.2017.09.014

De Vleeschouwer, D., Dunlea, A. G., Auer, G., Anderson, C. H., Brumsack, H., de Loach, A., et al. (2017). Quantifying K, U, and T h contents of marine sediments using shipboard natural gamma radiation spectra measured on DV JOIDES Resolution. *Geochemistry, Geophysics, Geosystems*, 18(3), 1053-1064. https://doi.org/10.1002/2016GC006715

De Vleeschouwer, D., Auer, G., Smith, R., Bogus, K., Christensen, B., Groeneveld, J., et al. (2018). The amplifying effect of Indonesian Throughflow heat transport on Late Pliocene Southern Hemisphere climate cooling. *Earth and Planetary Science Letters*, 500, 15-27. https://doi.org/10.1016/j.epsl.2018.07.035

Ding, Z. L., Derbyshire, E., Yang, S. L., Yu, Z. W., Xiong, S. F., & Liu, T. S. (2002). Stacked 2.6-Ma grain size record from the Chinese loess based on five sections and correlation with the deep-sea $\delta^{18}O$ record. *Paleoceanography*, 17(3), 5-1. https://doi.org/10.1029/2001PA000725

Ekström, M., McTainsh, G. H., & Chappell, A. (2004). Australian dust storms: temporal trends and relationships with synoptic pressure distributions (1960–99). *International Journal of Climatology: A Journal of the Royal Meteorological Society*, 24(12), 1581-1599. https://doi.org/10.1002/joc.1072

Ellis, B., Grant, K., Mallela, J., & Abram, N. (2019). Is XRF core scanning a viable method for coral palaeoclimate temperature reconstructions?. *Quaternary International*, 514, 97-107. https://doi.org/10.1016/j.quaint.2018.11.044

Elmore, A. C. , Mcclymont, E. L. , Elderfield, H. , Kender, S. , Cook, M. R. , & Leng, M. J. , et al. (2015). Antarctic intermediate water properties since 400 ka recorded in infaunal (*Uvigerina peregrina*) and epifaunal (*Planulina wuellerstorfi*) benthic foraminifera. *Earth and Planetary Science Letters*, 428(15), 193-203. https://doi.org/10.1016/j.epsl.2015.07.013

Feely, R. A., Sabine, C. L., Lee, K., Berelson, W., Kleypas, J., Fabry, V. J., & Millero, F. J. (2004). Impact of anthropogenic CO_2 on the $CaCO_3$ system in the oceans. *Science*, 305(5682), 362-366. https://doi.org/10.1126/science.1097329

Fieux, M., C., Andrié, E., & Charriaud, et al. (1996). Hydrological and chlorofluoromethane measurements of the indonesian throughflow entering the indian ocean. *Journal of Geophysical Research Oceans*, 101(C5), 12433– 12454. https://doi.org/10.1029/96JC00207

Fu, X., Cohen, T. J., & Arnold, L. J. (2017). Extending the record of lacustrine phases beyond the last interglacial for Lake Eyre in central Australia using luminescence dating. *Quaternary Science Reviews*, 162, 88-110. http://dx.doi.org/10.1016/j.quascirev.2017.03.002

Gallagher, S.J., Wallace, M.W., Hoiles, P.W. & Southwood, J. M. 2014. Seismic and stratigraphic evidence for reef expansion and onset of aridity on the Northwest Shelf of

Australia during the Pleistocene. *Marine and Petroleum Geology* v. 57, 470-481. 10.1016/j.marpetgeo.2014.06.011

Gallagher, S.J., Fulthorpe, C.S., Bogus, K., Auer, G., Baranwal, S., Castañeda, I.S., et al. (2017a). Site U1464. In Gallagher, S.J., Fulthorpe, C.S., Bogus, K., and the Expedition 356 Scientists, *Indonesian Throughflow*. Proceedings of the International Ocean Discovery Program, 356: College Station, TX (International Ocean Discovery Program). http://dx.doi.org/10.14379/iodp.proc.356.109.2017

Gallagher, S.J., Fulthorpe, C.S., Bogus, K., Auer, G., Baranwal, S., Castañeda, I.S., et al. (2017b). Site U1463. In Gallagher, S.J., Fulthorpe, C.S., Bogus, K., and the Expedition 356 Scientists, *Indonesian Throughflow*. Proceedings of the International Ocean Discovery Program, 356: College Station, TX (International Ocean Discovery Program). http://dx.doi.org/10.14379/iodp.proc.356.108.2017

Gallagher, S.J., Reuning, L., Himmler, T., Henderiks, J., De Vleeschouwer, D., Groeneveld, J., et al. (2018). The enigma of rare Quaternary oolites in the Indian and Pacific Oceans: a result of global oceanographic physicochemical conditions or a sampling bias. *Quaternary Science Reviews*, 200, 114-122. http://doi.org/10.1016/j.quascirev.2018.09.028

Gallagher, S.J. & deMenocal, P.B. (2019). Finding dry spells in Ocean Sediments. *Oceanography*, 32 (1), 38-41. https://doi.org/10.5670/oceanog.2019.120

Gallagher, S. J., & Wagstaff, B. E. (2021). Quaternary environments and monsoonal climate off northwest Australia: Palynological evidence from Ocean Drilling Program Site 765. *Quaternary Science Reviews*, 259, 106917. https://doi.org/10.1016/j.quascirev.2021.106917

Ganopolski, A., Rahmstorf, S., Petoukhov, V., & Claussen, M. (1998). Simulation of modern and glacial climates with a coupled global model of intermediate complexity. *Nature*, 391(6665), 351-356. https://doi.org/10.1038/34839

Grant, K. M., Amarathunga, U., Amies, J. D., Hu, P., Qian, Y., Penny, T., et al. (2022). Organic carbon burial in Mediterranean sapropels intensified during Green Sahara Periods since 3.2 Myr ago. *Communications Earth & Environment*, 3(1), 11. https://doi.org/10.1038/s43247-021-00339-9

Grinsted, A., Moore, J. C., & Jevrejeva, S. (2004). Application of the cross wavelet transform and wavelet coherence to geophysical time series. *Nonlinear Processes in Geophysics*, 11(5/6), 561-566. https://doi.org/10.5194/npg-11-561-2004

Groeneveld, J., De Vleeschouwer, D., McCaffrey, J. C., & Gallagher, S. J. (2021). Dating the northwest shelf of Australia since the Pliocene. *Geochemistry, Geophysics, Geosystems*, 22(3), e2020GC009418. https://doi.org/10.1029/2020GC009418

Hallenberger, M., Reuning, L., Gallagher, S. J., Back, S., Ishiwa, T., Christensen, B. A., & Bogus, K. (2019). Increased fluvial runoff terminated inorganic aragonite precipitation on the Northwest Shelf of Australia during the early Holocene. *Scientific Reports*, 9(1), 18356. https://doi.org/10.1038/s41598-019-54981-7

Hallenberger, M., Reuning, L., Back, S., Gallagher, S. J., Iwatani, H., & Lindhorst, K. (2022). Climate and sea-level controlling internal architecture of a Quaternary carbonate ramp (Northwest Shelf of Australia). *Sedimentology*, 69(3), 1276-1300. https://doi.org/10.1111/sed.12948

Hennekam, R., Grant, K. M., Rohling, E. J., Tjallingii, R., Heslop, D., Roberts, A. P., et al. (2022). Accurately calibrated XRF-CS record of Ti/Al reveals Early Pleistocene aridity/humidity variability over North Africa and its close relationship to low-latitude insolation. *Climate of the Past*, 18(11), 2509–2521. https://doi.org/10.5194/cp-18-2509-2022

Herraiz-Borreguero, L., & Rintoul, S. R. (2011). Subantarctic mode water: distribution and circulation. *Ocean Dynamics*, 61(1), 103-126. https://doi.org/10.1007/s10236-010-0352-9

Hesse, P. P., Magee, J. W., & van der Kaars, S. (2004). Late Quaternary climates of the Australian arid zone: a review. *Quaternary International*, 118, 87-102. https://doi.org/10.1016/S1040-6182(03)00132-0

Hinnov, L. A. (2000). New perspectives on orbitally forced stratigraphy. *Annual Review of Earth and Planetary Sciences*, 28(1), 419-475. https://doi.org/10.1146/annurev.earth.28.1.419

Holbourn, A., Kuhnt, W., Kawamura, H., Jian, Z., Grootes, P., Erlenkeuser, H., & Xu, J. (2005). Orbitally paced paleoproductivity variations in the Timor Sea and Indonesian Throughflow variability during the last 460 kyr. *Paleoceanography*, 20(3). https://doi.org/10.1029/2004PA001094

Hovan, S. A., Rea, D. K., & Pisias, N. G. (1991). Late Pleistocene continental climate and oceanic variability recorded in northwest Pacific sediments. *Paleoceanography*, 6(3), 349-370. https://doi.org/10.1029/91PA00559

Imbrie, J., Hays, J.D., Martinson, D.B., McIntyre, A., Mix, A.C., Morlet, J.J., et al. (1984). The orbital theory of Pleistocene climate: support from a revised chronology of the marine $\delta^{18}O$

record. In: Berger, A., et al. (Eds.), *Milankovitch and Climate* (part 1, pp. 269–305). D. Reidel Publishing Company.

Kalnay, E., Kanamitsu, M., Kistler, R., Collins, W., Deaven, D., Gandin, L., et al. (1996). The NCEP/NCAR 40-year reanalysis project. *Bulletin of the American Meteorological Society*, 77(3), 437-472. https://doi.org/10.1175/1520-0477(1996)077<0437:TNYRP>2.0.CO;2

Keil, R. (2017). Anthropogenic forcing of carbonate and organic carbon preservation in marine sediments. *Annual Review of Marine Science*, 9, 151-172. https://doi.org/10.1146/annurev-marine-010816-060724

Kershaw, A. P., van der Kaars, S., & Moss, P. T. (2003). Late Quaternary Milankovitch-scale climatic change and variability and its impact on monsoonal Australasia. *Marine Geology*, 201(1-3), 81-95. https://doi.org/10.1016/S0025-3227(03)00210-X

Key, R.M., Olsen, A., van Heuven, S., Lauvset, S. K., Velo, A., Lin, X., et al. (2015). *Global Ocean Data Analysis Project, Version 2 (GLODAPv2), ORNL/CDIAC-162, NDP-093*. Carbon Dioxide Information Analysis Center, Oak Ridge National Laboratory, US Department of Energy, Oak Ridge, Tennessee. https://doi.org/10.3334/CDIAC/OTG.NDP093_GLODAPv2

Kleypas, J. A., Buddemeier, R. W., Archer, D., Gattuso, J. P., Langdon, C., & Opdyke, B. N. (1999). Geochemical consequences of increased atmospheric carbon dioxide on coral reefs. *Science*, 284(5411), 118-120. https://doi.org/10.1126/science.284.5411.118

Kochhann, K. G., Holbourn, A., Kuhnt, W., Channell, J. E., Lyle, M., Shackford, J. K., et al. (2016). Eccentricity pacing of eastern equatorial Pacific carbonate dissolution cycles during the Miocene Climatic Optimum. *Paleoceanography*, 31(9), 1176-1192. https://doi.org/10.1002/2016PA002988

Kuhnt, W., Holbourn, A., Xu, J., Opdyke, B., De Deckker, P., Röhl, U., & Mudelsee, M. (2015). Southern Hemisphere control on Australian monsoon variability during the late deglaciation and Holocene. *Nature Communications*, 6(1), 5916. https://doi.org/10.1038/ncomms6916

Larrasoaña, J. C., Roberts, A. P., Rohling, E. J., Winklhofer, M., & Wehausen, R. (2003). Three million years of monsoon variability over the northern Sahara. *Climate Dynamics*, 21(7-8), 689-698. https://doi.org/10.1007/s00382-003-0355-z

Laskar, J., Robutel, P., Joutel, F., Gastineau, M., Correia, A. C. M., & Levrard, B. (2004). A long-term numerical solution for the insolation quantities of the Earth. *Astronomy & Astrophysics*, 428(1), 261-285. https://doi.org/10.1051/0004-6361:20041335

Leuschner, D. C., & Sirocko, F. (2003). Orbital insolation forcing of the Indian Monsoon–a motor for global climate changes?. *Palaeogeography, Palaeoclimatology, Palaeoecology*, 197(1-2), 83-95. https://doi.org/10.1016/S0031-0182(03)00387-0

Lewis, E. & Wallace, D. W. R. (1998). Program Developed for CO2 System Calculations, ORNL/CDIAC-105, Carbon Dioxide Inf. Anal. Cent., Oak Ridge Natl. Lab., Oak Ridge, Tenn., 38 pp.

Liebrand, D., Beddow, H. M., Lourens, L. J., Pälike, H., Raffi, I., Bohaty, S. M., et al. (2016). Cyclostratigraphy and eccentricity tuning of the early Oligocene through early Miocene (30.1–17.1 Ma): Cibicides mundulus stable oxygen and carbon isotope records from Walvis Ridge Site 1264. *Earth and Planetary Science Letters*, 450, 392-405. https://doi.org/10.1016/j.epsl.2016.06.007

Liu, Y., Lo, L., Shi, Z., Wei, K. Y., Chou, C. J., Chen, Y. C., et al. (2015). Obliquity pacing of the western Pacific Intertropical Convergence Zone over the past 282,000 years. *Nature Communications*, 6(1), 1-7. https://doi.org/10.1038/ncomms10018

Mackensen, A., & Schmiedl, G. (2019). Stable carbon isotopes in paleoceanography: atmosphere, oceans, and sediments. *Earth-Science Reviews*, 197, 102893. https://doi.org/10.1016/j.earscirev.2019.102893

Magee, J. W., Miller, G. H., Spooner, N. A., & Questiaux, D. (2004). Continuous 150 ky monsoon record from Lake Eyre, Australia: insolation-forcing implications and unexpected Holocene failure. *Geology*, 32(10), 885-888. https://doi.org/10.1130/G20672.1

Mantsis, D. F., Lintner, B. R., Broccoli, A. J., Erb, M. P., Clement, A. C., & Park, H. S. (2014). The response of large-scale circulation to obliquity-induced changes in meridional heating gradients. *Journal of Climate*, 27(14), 5504-5516. https://doi.org/10.1175/JCLI-D-13-00526.1

McClymont, E. L., Elmore, A. C., Kender, S., Leng, M. J., Greaves, M., & Elderfield, H. (2016). Pliocene-Pleistocene evolution of sea surface and intermediate water temperatures from the southwest Pacific. *Paleoceanography*, 31(6), 895-913. https://doi.org/10.1002/2016PA002954

McGowan, H., & Clark, A. (2008). Identification of dust transport pathways from Lake Eyre, Australia using Hysplit. *Atmospheric Environment*, 42(29), 6915-6925. https://doi.org/10.1016/j.atmosenv.2008.05.053

McTainsh, G. H. (1989). Quaternary aeolian dust processes and sediments in the Australian region. *Quaternary Science Reviews*, 8(3), 235-253. https://doi.org/10.1016/0277-3791(89)90039-5

Mélice, J. L., Coron, A., & Berger, A. (2001). Amplitude and frequency modulations of the Earth's obliquity for the last million years. *Journal of Climate*, 14(6), 1043-1054. https://doi.org/10.1175/1520-0442(2001)014<1043:AAFMOT>2.0.CO;2

Miller, G., Mangan, J., Pollard, D., Thompson, S., Felzer, B., & Magee, J. (2005). Sensitivity of the Australian Monsoon to insolation and vegetation: implications for human impact on continental moisture balance. *Geology*, 33(1), 65-68. https://doi.org/10.1130/G21033.1

Miller, G. H., Magee, J. W., Fogel, M. L., Wooller, M. J., Hesse, P. P., Spooner, N. A., et al. (2018). Wolfe Creek Crater: A continuous sediment fill in the Australian Arid Zone records changes in monsoon strength through the Late Quaternary. *Quaternary Science Reviews*, 199, 108-125. https://doi.org/10.1016/j.quascirev.2018.07.019

Moore Jr, T. C., Pisias, N. G., & Dunn, D. A. (1982). Carbonate time series of the Quaternary and late Miocene sediments in the Pacific Ocean: a spectral comparison. *Marine Geology*, 46(3-4), 217-233. https://doi.org/10.1016/0025-3227(82)90081-0

Pälike, H., Norris, R. D., Herrle, J. O., Wilson, P. A., Coxall, H. K., Lear, C. H., et al. (2006). The heartbeat of the Oligocene climate system. *Science*, 314(5807), 1894-1898. https://doi.org/10.1126/science.1133822

Pei, R., Kuhnt, W., Holbourn, A., Hingst, J., Koppe, M., Schultz, J., et al. (2021). Monitoring Australian Monsoon variability over the past four glacial cycles. *Palaeogeography, Palaeoclimatology, Palaeoecology*, 568, 110280. https://doi.org/10.1016/j.palaeo.2021.110280

Pisias, N. G., & Rea, D. K. (1988). Late Pleistocene paleoclimatology of the central equatorial Pacific: Sea surface response to the southeast trade winds. *Paleoceanography*, 3(1), 21-37. https://doi.org/10.1029/PA003i001p00021

Rayner, N. A. A., Parker, D. E., Horton, E. B., Folland, C. K., Alexander, L. V., Rowell, D. P., et al. (2003). Global analyses of sea surface temperature, sea ice, and night marine air temperature since the late nineteenth century. *Journal of Geophysical Research: Atmospheres*, 108(D14). https://doi.org/10.1029/2002JD002670

Reichart, G.-J. (1997). Late Quaternary variability of the Arabian Sea monsoon and oxygen minimum zone (Ph.D. thesis). Retrieved from http://dspace.library.uu.nl/handle/1874/274419. Netherlands: Utrecht University.

Rial, J. A. (1999). Pacemaking the ice ages by frequency modulation of Earth's orbital eccentricity. *Science*, 285(5427), 564-568. https://www.science.org/doi/10.1126/science.285.5427.564

Rial, J. A., & Anaclerio, C. A. (2000). Understanding nonlinear responses of the climate system to orbital forcing. *Quaternary Science Reviews*, 19(17-18), 1709-1722. https://doi.org/10.1016/S0277-3791(00)00087-1

Richardson, L. E., Middleton, J. F., Kyser, T. K., James, N. P., & Opdyke, B. N. (2019). Shallow water masses and their connectivity along the southern Australian continental margin. *Deep Sea Research Part I: Oceanographic Research Papers*, 152, 103083. https://doi.org/10.1016/j.dsr.2019.103083

Ridgway, K. R. , & Godfrey, J. S. . (2015). The source of the Leeuwin Current seasonality. *Journal of Geophysical Research Oceans*, 120(10), 6843-6864. https://doi.org/10.1002/2015JC011049

Rohling, E. J., Yu, J., Heslop, D., Foster, G. L., Opdyke, B., & Roberts, A. P. (2021). Sea level and deep-sea temperature reconstructions suggest quasi-stable states and critical transitions over the past 40 million years. *Science Advances*, 7(26), eabf5326. https://doi.org/10.1126/sciadv.abf5326

Rothwell, R. G. & Croudace, I. W. (2015). Twenty years of XRF core scanning marine sediments: what do geochemical proxies tell us?. In *Micro-XRF Studies of Sediment Cores* (pp. 25-102). Springer, Dordrecht.

Santer, B. D., Wigley, T. M. L., Boyle, J. S., Gaffen, D. J., Hnilo, J. J., Nychka, D., et al. (2000). Statistical significance of trends and trend differences in layer-average atmospheric temperature time series. *Journal of Geophysical Research: Atmospheres*, 105(D6), 7337-7356. https://doi.org/10.1029/1999JD901105

Schneider, U., Becker, A., Finger, P., Meyer-Christoffer, A., Rudolf, B., & Ziese, M. (2011). GPCC Full Data Reanalysis Version 6.0 at 0.5°: Monthly Land-Surface Precipitation from Rain-Gauges built on GTS-based and Historic Data. https://doi.org/10.5676/DWD_GPCC/FD_M_V7_050

Schulz, M., & Mudelsee, M. (2002). REDFIT: estimating red-noise spectra directly from unevenly spaced paleoclimatic time series. *Computers & Geosciences*, 28(3), 421-426. https://doi.org/10.1016/S0098-3004(01)00044-9

Schwendike, J., Govekar, P., Reeder, M. J., Wardle, R., Berry, G. J., & Jakob, C. (2014). Local partitioning of the overturning circulation in the tropics and the connection to the Hadley and Walker circulations. *Journal of Geophysical Research: Atmospheres*, 119(3), 1322-1339. https://doi.org/10.1002/2013JD020742

Shi, Z. G., Liu, X. D., Sun, Y. B., An, Z. S., Liu, Z., & Kutzbach, J. (2011). Distinct responses of East Asian summer and winter monsoons to astronomical forcing. *Climate of the Past*, 7(4), 1363-1370. https://doi.org/10.5194/cp-7-1363-2011

Strong, C. L., Parsons, K., McTainsh, G. H., & Sheehan, A. (2011). Dust transporting wind systems in the lower Lake Eyre Basin, Australia: A preliminary study. *Aeolian Research*, 2(4), 205-214. https://doi.org/10.1016/j.aeolia.2010.11.001

Stuut, J. B. W., Temmesfeld, F., & De Deckker, P. (2014). A 550 ka record of aeolian activity near North West Cape, Australia: inferences from grain-size distributions and bulk chemistry of SE Indian Ocean deep-sea sediments. *Quaternary Science Reviews*, 83, 83-94. https://doi.org/10.1016/j.quascirev.2013.11.003

Stuut, J. B. W., De Deckker, P., Saavedra-Pellitero, M., Bassinot, F., Drury, A. J., Walczak, M. H., et al. (2019). A 5.3-million-year history of monsoonal precipitation in northwestern Australia. *Geophysical Research Letters*, 46(12), 6946-6954. https://doi.org/10.1029/2019GL083035

Sun, Y., Clemens, S. C., An, Z., & Yu, Z. (2006). Astronomical timescale and palaeoclimatic implication of stacked 3.6-Myr monsoon records from the Chinese Loess Plateau. *Quaternary Science Reviews*, 25(1-2), 33-48. https://doi.org/10.1016/j.quascirev.2005.07.005

Suppiah, R. (1992). The Australian summer monsoon: A review. *Progress in Physical Geography*, 16(3), 283-318. https://doi.org/10.1177/030913339201600302

Suppiah, R., & Wu, X. (1998). Surges, cross-equatorial flows and their links with the Australian summer monsoon circulation and rainfall. *Australian Meteorological Magazine* 47, 113-130.

Talley, L. D., & Sprintall, J. (2005). Deep expression of the Indonesian Throughflow: Indonesian intermediate water in the South Equatorial Current. *Journal of Geophysical Research: Oceans*, 110(C10). https://doi.org/10.1029/2004JC002826

Taylor, J.R. (1997). *Introduction to Error Analysis, the Study of Uncertainties in Physical Measurements, 2nd Edition*. Sausalito, California: University Science Books.

Thompson, P. R., Bé, A. W., Duplessy, J. C., & Shackleton, N. J. (1979). Disappearance of pink-pigmented Globigerinoides ruber at 120,000 yr BP in the Indian and Pacific Oceans. *Nature*, 280(5723), 554-558. https://doi.org/10.1038/280554a0

Thomson, D. J. (1982). Spectrum estimation and harmonic analysis. *Proceedings of the IEEE*, 70(9), 1055-1096. https://doi.org/10.1109/PROC.1982.12433

Turner, S. K. (2014). Pliocene switch in orbital-scale carbon cycle/climate dynamics. *Paleoceanography*, 29(12), 1256-1266. https://doi.org/10.1002/2014PA002651

Verosub, K. L., & Roberts, A. P. (1995). Environmental magnetism: Past, present, and future. *Journal of Geophysical Research: Solid Earth*, 100(B2), 2175-2192. https://doi.org/10.1029/94JB02713

Wade, B. S., Pearson, P. N., Berggren, W. A., & Pälike, H. (2011). Review and revision of Cenozoic tropical planktonic foraminiferal biostratigraphy and calibration to the geomagnetic polarity and astronomical time scale. *Earth-Science Reviews*, 104(1-3), 111-142. https://doi.org/10.1016/j.earscirev.2010.09.003

Wang, P., Tian, J., & Lourens, L. J. (2010). Obscuring of long eccentricity cyclicity in Pleistocene oceanic carbon isotope records. *Earth and Planetary Science Letters*, 290(3-4), 319-330. https://doi.org/10.1016/j.epsl.2009.12.028

Weltje, G. J., Bloemsma, M. R., Tjallingii, R., Heslop, D., Röhl, U., & Croudace, I. W. (2015). Prediction of geochemical composition from XRF core scanner data: a new multivariate approach including automatic selection of calibration samples and quantification of uncertainties. In *Micro-XRF Studies of Sediment Cores* (pp. 507-534). Springer, Dordrecht.

Wijeratne, S., Pattiaratchi, C., & Proctor, R. (2018). Estimates of surface and subsurface boundary current transport around Australia. *Journal of Geophysical Research: Oceans*, 123(5), 3444-3466. https://doi.org/10.1029/2017JC013221

Wong, A. P. (2005). Subantarctic mode water and Antarctic intermediate water in the south Indian Ocean based on profiling float data 2000–2004. *Journal of Marine Research*, 63(4), 789-812. https://elischolar.library.yale.edu/journal_of_marine_research/101

Woo, M., & Pattiaratchi, C. (2008). Hydrography and water masses off the western Australian coast. *Deep Sea Research Part I: Oceanographic Research Papers*, 55(9), 1090-1104.

Wyrwoll, K. H., & Valdes, P. (2003). Insolation forcing of the Australian monsoon as controls of Pleistocene mega-lake events. *Geophysical Research Letters*, 30(24). https://doi.org/10.1029/2003GL018486

Wyrwoll, K. H., Liu, Z., Chen, G., Kutzbach, J. E., & Liu, X. (2007). Sensitivity of the Australian summer monsoon to tilt and precession forcing. *Quaternary Science Reviews*, 26(25-28), 3043-3057. https://doi.org/10.1016/j.quascirev.2007.06.026

Zenk, W., Siedler, G., Ishida, A., Holfort, J., Kashino, Y., Kuroda, Y., et al. (2005). Pathways and variability of the Antarctic Intermediate Water in the western equatorial Pacific Ocean. *Progress in Oceanography*, 67(1-2), 245-281. https://doi.org/10.1016/j.pocean.2005.05.003

Zhang, P., Xu, J., Holbourn, A., Kuhnt, W., Beil, S., Li, T., et al. (2020). Indo-Pacific Hydroclimate in Response to Changes of the Intertropical Convergence Zone: Discrepancy on Precession and Obliquity Bands Over the Last 410 kyr. *Journal of Geophysical Research: Atmospheres*, 125(14), e2019JD032125. https://doi.org/10.1029/2019JD032125

Zhang, P., Xu, J., Holbourn, A., Kuhnt, W., Xiong, Z., & Li, T. (2022). Obliquity induced latitudinal migration of the Intertropical Convergence Zone during the past ∼410 kyr. *Geophysical Research Letters*, 49(21), e2022GL100039. https://doi.org/10.1029/2022GL100039

Zhao, S., & Grant, K. (2023). Data for "Early-Pleistocene orbital variability in Northwest Australian shelf sediments" submitted to Paleoceanography and Paleoclimatology [Dataset]. Zenodo. https://doi.org/10.5281/zenodo.10360338

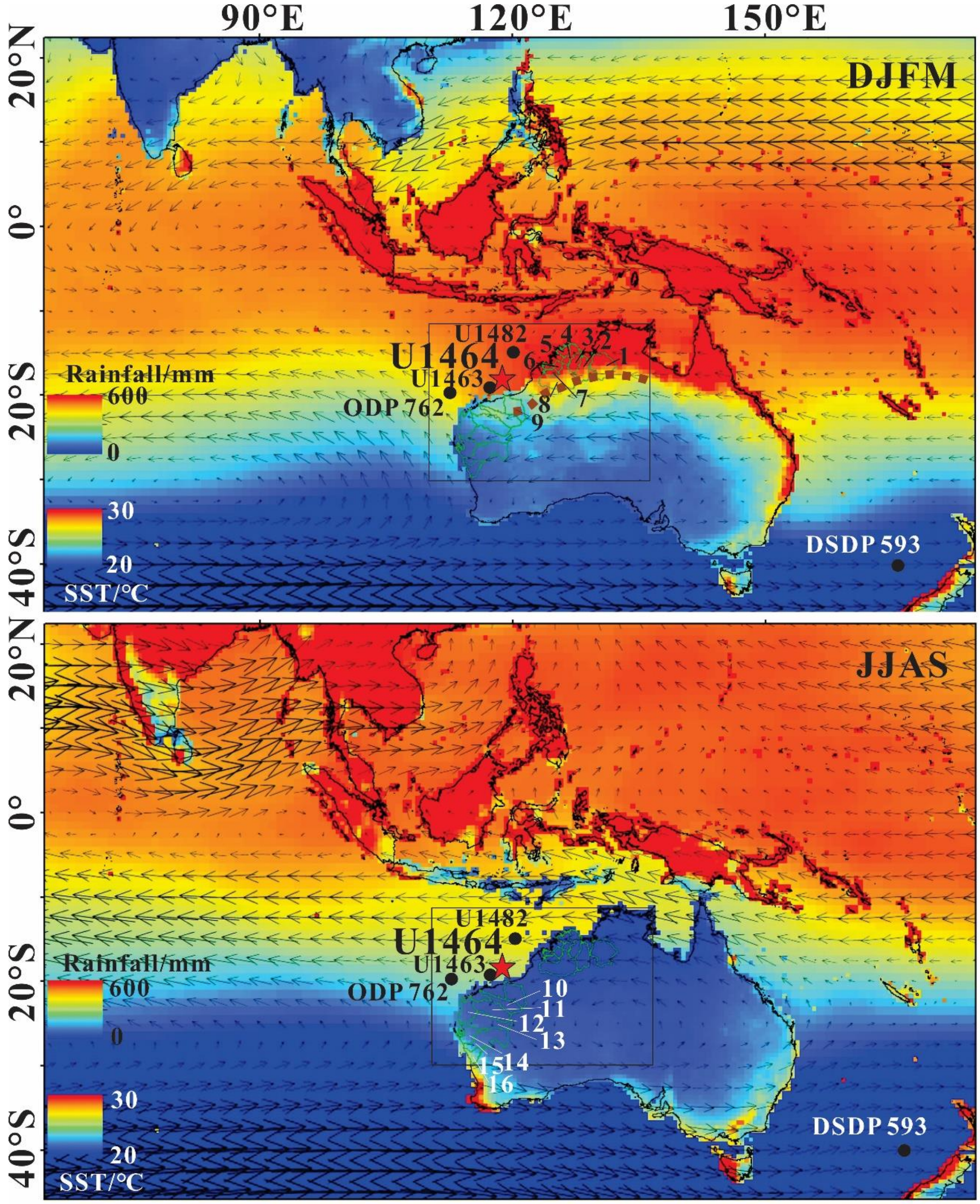

90°E
120°E
150°E
20°N
0°
20°S
40°S
DJFM
JJAS
U1464
U1463
U1482
ODP 762
DSDP 593
Rainfall/mm
600
0
SST/°C
30
20
1
2
3
4
5
6
7
8
9
10
11
12
13
14
15
16

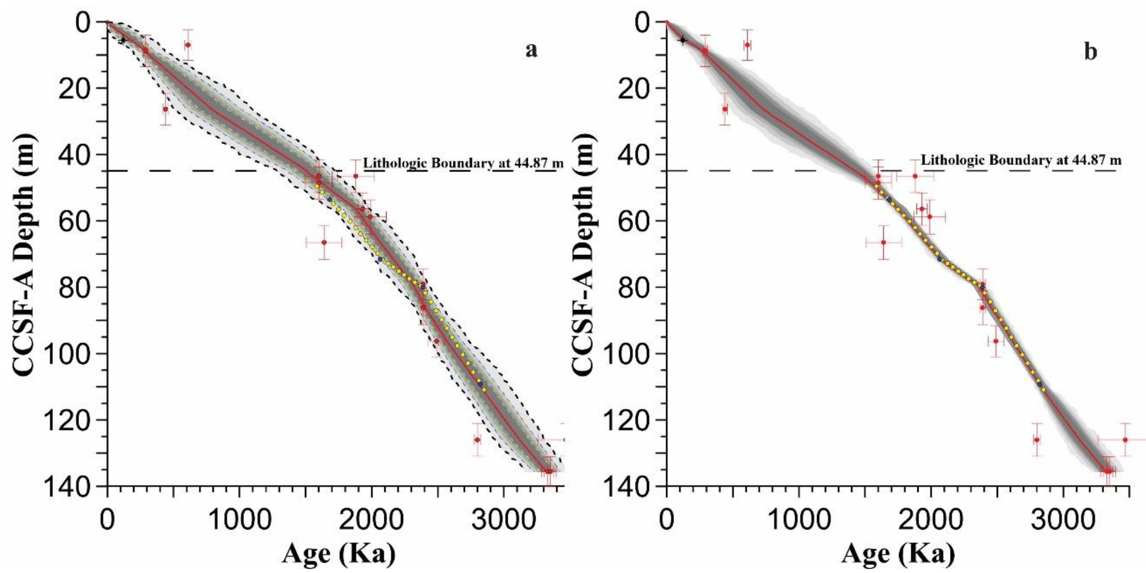
a
b
Lithologic Boundary at 44.87 m
CCSF-A Depth (m)
Age (Ka)
0
20
40
60
80
100
120
140
0
1000
2000
3000

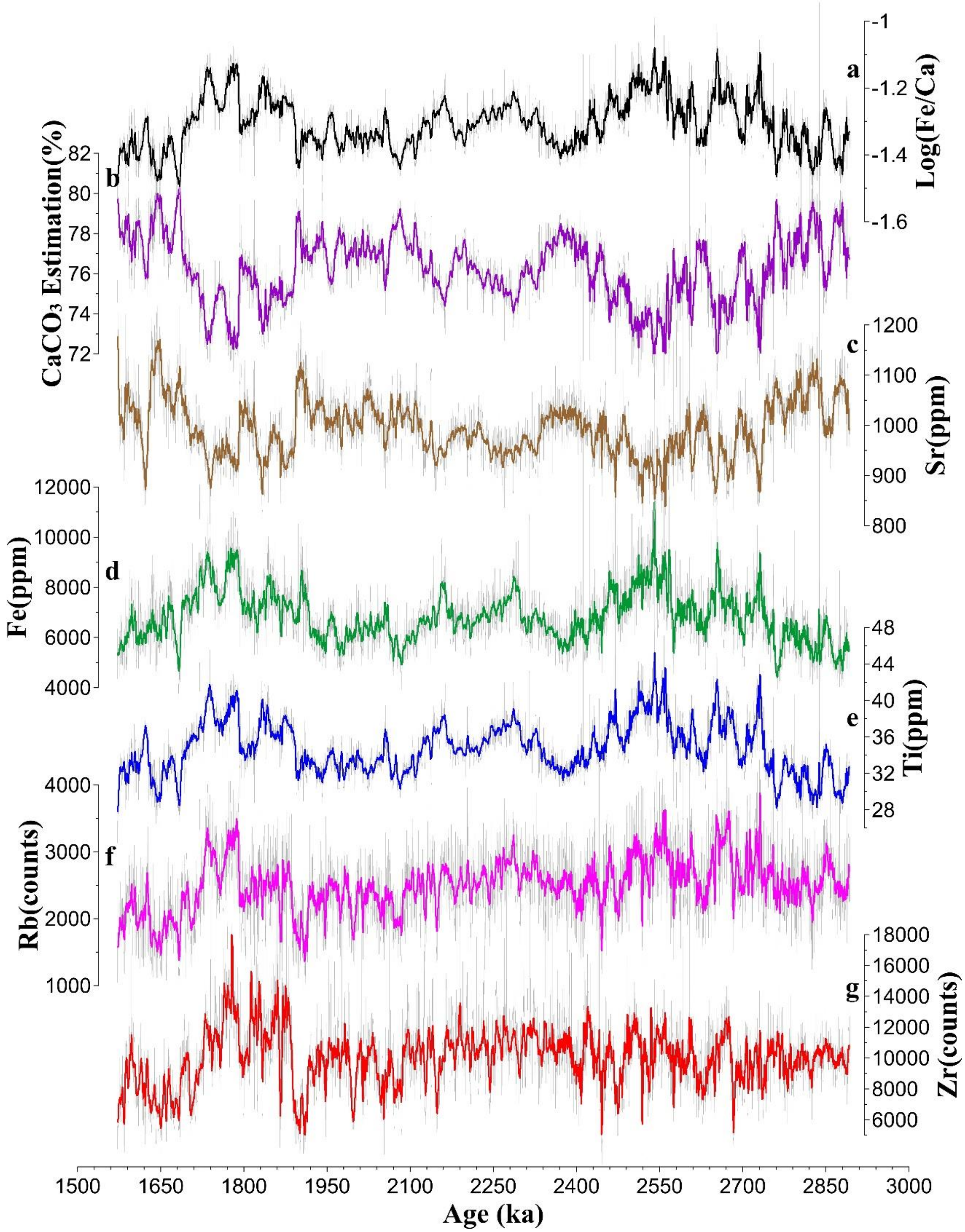

a
Log(Fe/Ca)
-1
-1.2
-1.4
-1.6
b
CaCO3 Estimation(%)
82
80
78
76
74
72
c
Sr(ppm)
1200
1100
1000
900
800
d
Fe(ppm)
12000
10000
8000
6000
4000
e
Ti(ppm)
48
44
40
36
32
28
f
Rb(counts)
4000
3000
2000
1000
g
Zr(counts)
18000
16000
14000
12000
10000
8000
6000
1500
1650
1800
1950
2100
2250
2400
2550
2700
2850
3000
Age (ka)

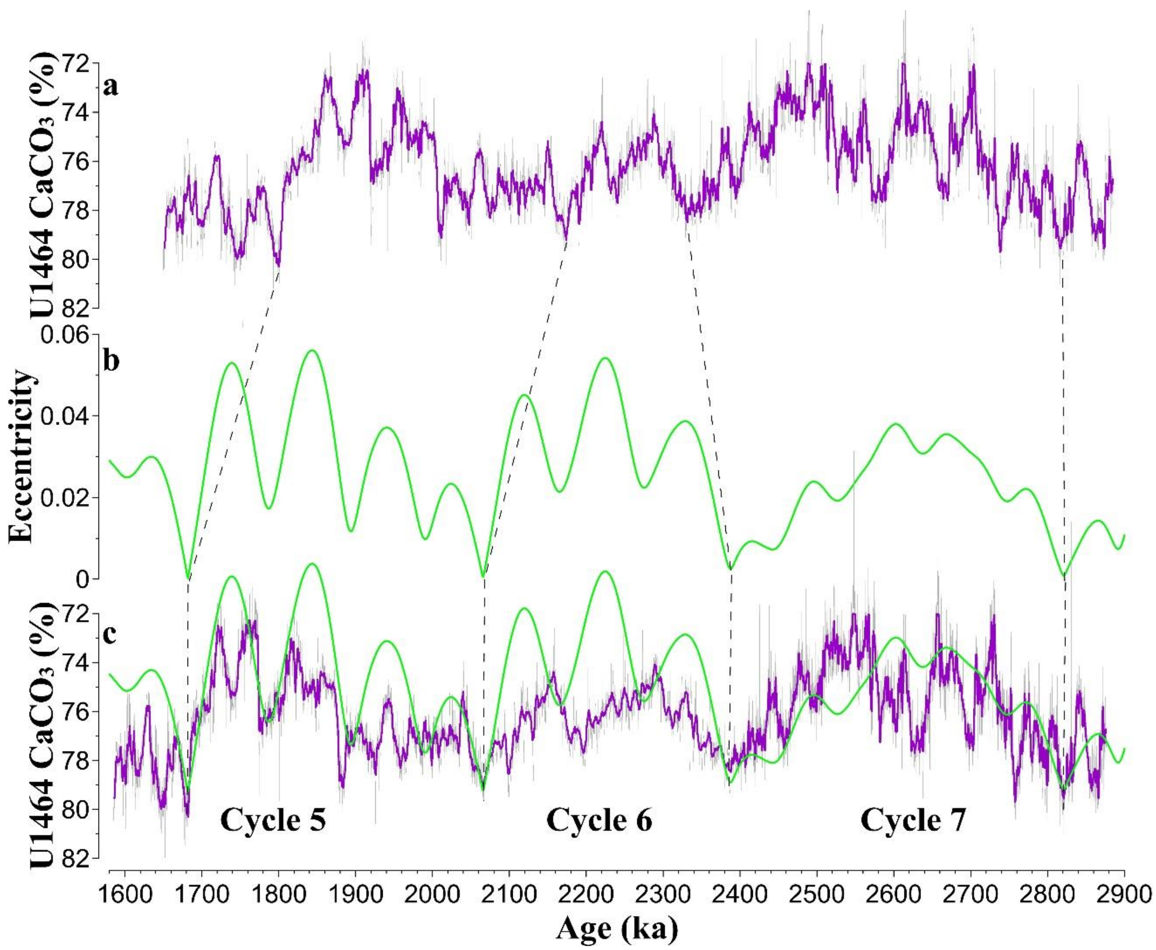
a
b
c
U1464 CaCO3 (%)
72
74
76
78
80
82
Eccentricity
0.06
0.04
0.02
0
U1464 CaCO3 (%)
72
74
76
78
80
82
Cycle 5
Cycle 6
Cycle 7
1600
1700
1800
1900
2000
2100
2200
2300
2400
2500
2600
2700
2800
2900
Age (ka)

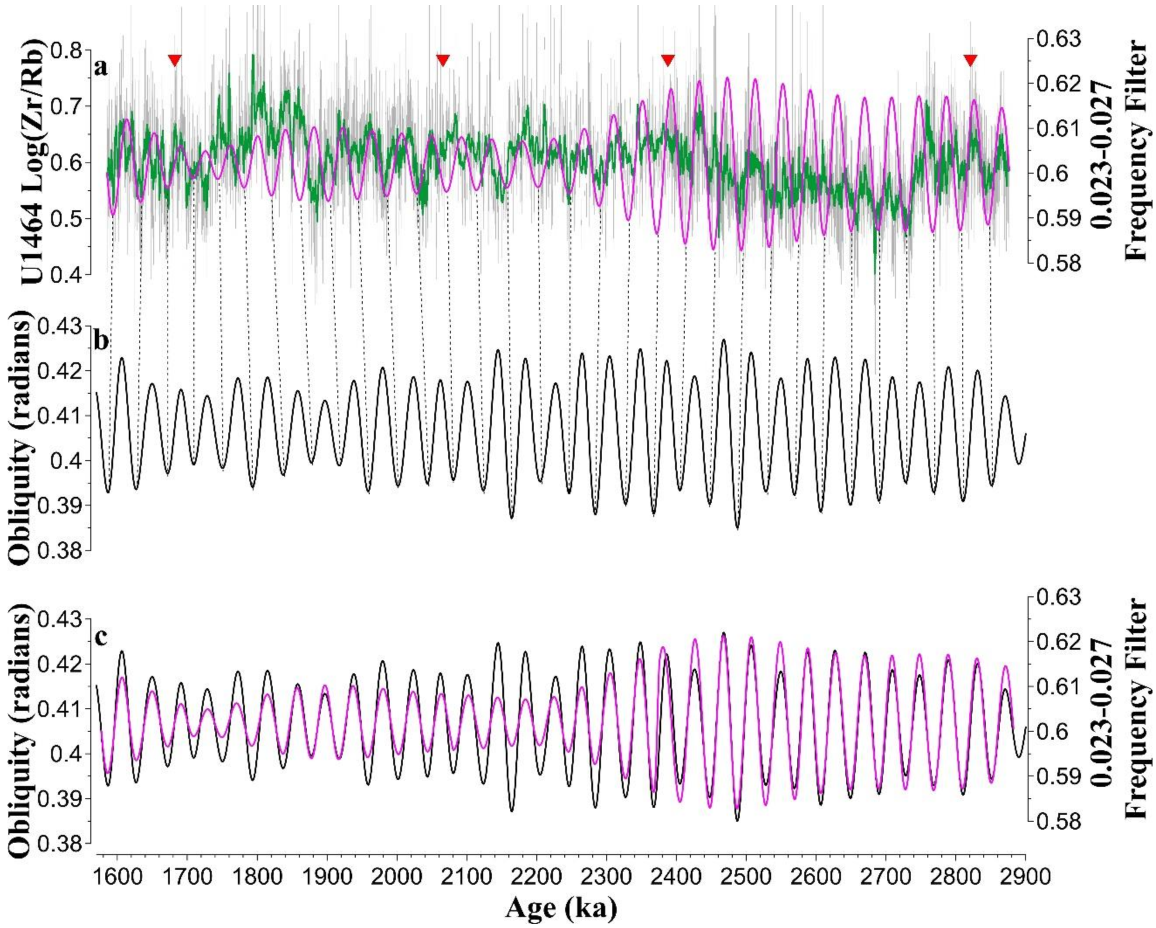

a
b
c
U1464 Log(Zr/Rb)
0.023-0.027 Frequency Filter
Obliquity (radians)
0.8
0.7
0.6
0.5
0.4
0.63
0.62
0.61
0.6
0.59
0.58
0.43
0.42
0.41
0.4
0.39
0.38
1600 1700 1800 1900 2000 2100 2200 2300 2400 2500 2600 2700 2800 2900
Age (ka)

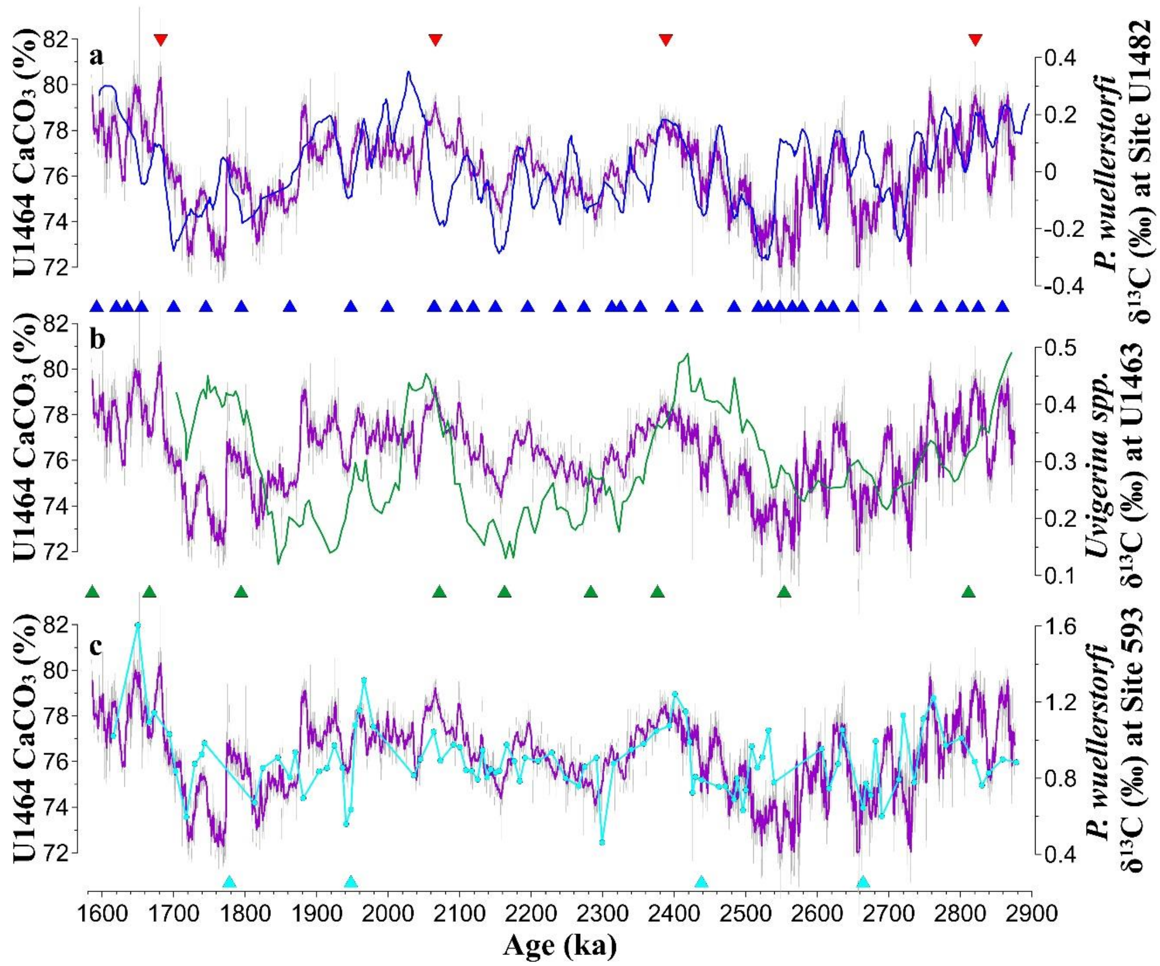

a
b
c
U1464 CaCO₃ (%)
P. wuellerstorfi δ13C (‰) at Site U1482
Uvigerina spp. δ13C (‰) at U1463
P. wuellerstorfi δ13C (‰) at Site 593
Age (ka)

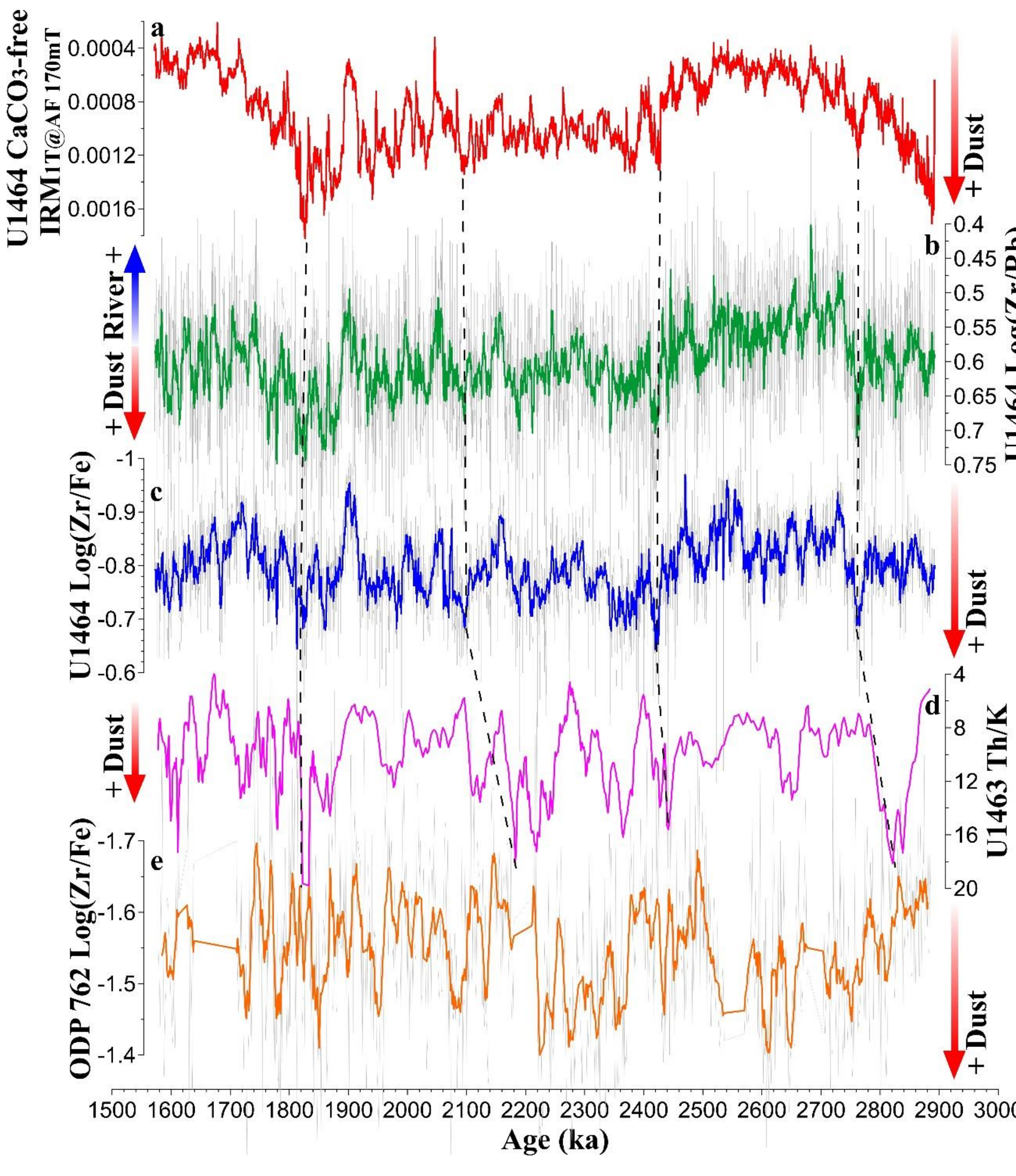

U1464 CaCO3-free
IRM1T@AF 170mT
a
0.0004
0.0008
0.0012
0.0016
+ Dust
b
0.4
0.45
0.5
0.55
0.6
0.65
0.7
0.75
U1464 Log(Zr/Rb)
+ Dust River +
c
-1
-0.9
-0.8
-0.7
-0.6
U1464 Log(Zr/Fe)
+ Dust
d
4
8
12
16
20
U1463 Th/K
+ Dust
e
-1.7
-1.6
-1.5
-1.4
ODP 762 Log(Zr/Fe)
+ Dust
1500
1600
1700
1800
1900
2000
2100
2200
2300
2400
2500
2600
2700
2800
2900
3000
Age (ka)

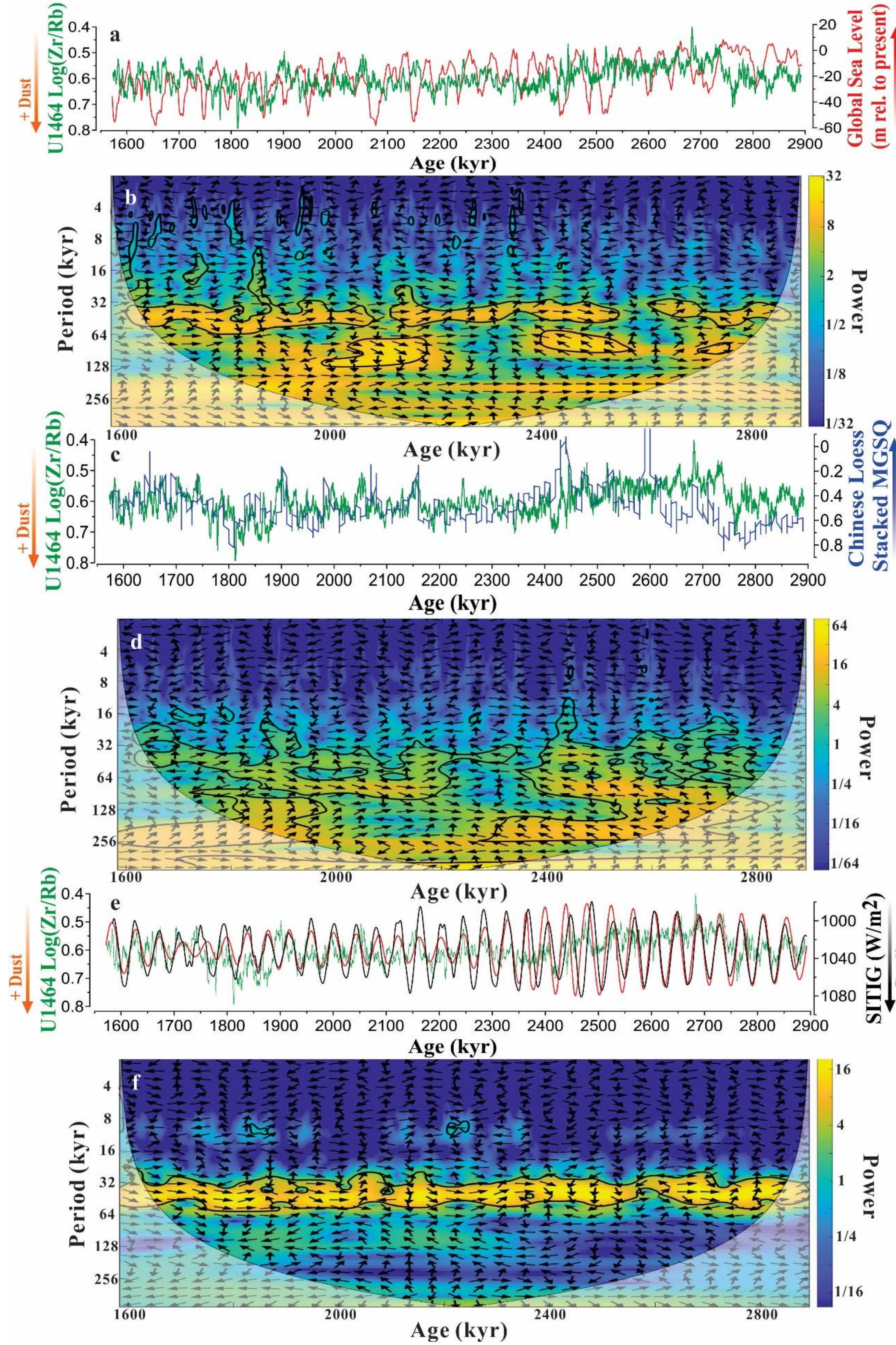

a
U1464 Log(Zr/Rb)
+ Dust
Global Sea Level (m rel. to present)
Rise +
Age (kyr)
b
Period (kyr)
Power
Age (kyr)
c
U1464 Log(Zr/Rb)
+ Dust
Chinese Loess Stacked MGSQ
EAWM +
Age (kyr)
d
Period (kyr)
Power
Age (kyr)
e
U1464 Log(Zr/Rb)
+ Dust
SITIG (W/m2)
+ Gradient
Age (kyr)
f
Period (kyr)
Power
Age (kyr)

Paleoceanography and Paleoclimatology

Supporting Information for

Early-Pleistocene orbital variability in Northwest Australian shelf sediments

Song Zhao[1], Katharine M. Grant[1], David Heslop[1], and Stephen Gallagher[2]

[1] Research School of Earth Sciences, Australian National University, Canberra, ACT, Australia.

[2] School of Geography, Earth and Atmospheric Sciences, University of Melbourne, Melbourne, Victoria, Australia.

Contents of this file

Text S1. Alternative eccentricity tunings

In order to fully consider the uncertainty of this eccentricity tuning, twelve scenarios have been found based on different options for each tie-point (Figure S5; Table S4). Pearson and Spearman correlation coefficients are calculated to show the linear and monotonic relationship between eccentricity and our $CaCO_3$ record (Figure S5). Correlation analyses suggest that 53.62, 71.57, 79.97 and 109.18 mbsf are the best four tie-points for the eccentricity minima at 1682, 2066, 2388 and 2821 kyr, respectively (Figure S5k; Table S4). Additionally, we have calculated the corresponding p value for each of the regressions in twelve scenarios to test if there is a more robust relationship between eccentricity and the U1464 $CaCO_3$ record.

Following previous studies (Santer et al., 2000), we estimate residuals in $CaCO_3$ based on the least squares linear regression with eccentricity (i.e., $e(x) = y(x) – \bar{y}(x)$, where e is the regression residual, y is the $CaCO_3$ and $\bar{y}$ is the regression of $CaCO_3$ (dependent variable) with eccentricity (independent variable), x is the eccentricity), and assess the autocorrelation in the residuals. We adjust the effective number of samples according to the autocorrelation and then calculate the p value. Basically, we first calculate the lag-1 autocorrelation coefficient of residuals (r_1) to obtain the effective number of samples (n_e) based on $n_e = n_t * (1 - r_1) / (1 + r_1)$, where n_t is the total number of samples. The variance of residuals (S_e^2) is given by $[1 / (n_e - 2)] * \sum_{n=1}^{nt} e(x)^2$, and the standard error of regression coefficient (b) is defined as $S_b = S_e / [\sum_{n=1}^{nt}(x - \bar{x})^2]^{1/2}$, where $\bar{x}$ is the eccentricity mean. Accordingly, the ratio between b and S_b can be used as the t value, and then substituted to the cumulative t-distribution with $n_e - 2$ degrees of freedom to get p values. The p value for option (k) is smallest one (Figure S5k), which corresponds with its highest correlation coefficients.

Text S2. Uncertainties in IODP Site U1464 dust proxy records

To quantify the potential influence of measurement uncertainties on the observed variability in our dust-flux proxy records, we calculate measurement uncertainties and their propagation in our Log(Zr/Rb), Log(Zr/Fe) and $CaCO_3$-free $IRM_{1T@AF\ 170mT}$ records. The principal formulas for error propagation in this study are as follows (Taylor, 1997):

(i) If q is any function of several variables x, …, z, then δq = sqrt (($\frac{\partial q}{\partial x}$ * δx)^2 + … + ($\frac{\partial q}{\partial z}$ * δz)^2), where variables x, …, z are measured with one standard deviation (1δ, expressed as δx, …, δz).

(ii) If q is the sum and difference, q = x + … + z – (u + … + w), then δq = sqrt ((δx)^2 + … + (δz)^2 + (δu)^2 + … + (δw)^2).

(iii) If q = Bx, where B is a known constant, then δq = |B|δx, where |B| is absolute value.

(iv) If q is the product and quotient, q = (x * … * z) / (u * … * w), then $\frac{\delta q}{|q|}$ = sqrt (($\frac{\delta x}{x}$)^2 + … + ($\frac{\delta z}{z}$)^2 + ($\frac{\delta u}{u}$)^2 + … + ($\frac{\delta w}{w}$)^2).

Based on equation (i), the 1δ of logarithm function (Log(x/y)) can be derived as follows: δLog(x/y) = sqrt (($\frac{1}{x}$ * δx)^2 + (- $\frac{1}{y}$ * δy)^2). In this study, the average fractional uncertainties (ratios of 1δ values to values of individual measurement) for Zr, Rb and Fe ($\frac{\delta Zr}{Zr}$, $\frac{\delta Rb}{Rb}$ and $\frac{\delta Fe}{Fe}$) are 0.033, 0.102 and 0.007, respectively. Accordingly, δLog(Zr/Rb) = sqrt (($\frac{1}{Zr}$ * δZr)^2 + (- $\frac{1}{Rb}$ * δRb)^2) = sqrt (0.033^2 + 0.102^2) = 0.107; δLog(Zr/Fe) = sqrt (($\frac{1}{Zr}$ * δZr)^2 + (- $\frac{1}{Fe}$ * δFe)^2) = sqrt (0.033^2 + 0.007^2) = 0.034. To obtain the 1δ of the n-point running average of Log(x/y), equations (ii) and (iii) are applied to divide the δLog(x/y) value by sqrt (n), where n is the number of data-points in the running average; i.e., δLog(x/y)$_{average}$ = (1/n) * sqrt ((δLog(x/y)$_1$)^2 + … + (δLog(x/y)$_n$)^2) = (1/n) * sqrt (n * (δLog(x/y))^2) =

δLog(x/y) / sqrt (n), where each δLog(x/y) is the same. We use a 21-point running average, which yields δLog(Zr/Rb)$_{average}$ = 0.107 / sqrt(21) = 0.023 and δLog(Zr/Fe)$_{average}$ = 0.034 / sqrt(21) = 0.007. We further multiply ±1δ values by 1.96 (2.58) to obtain the 95 % (99 %) confidence intervals for Log(Zr/Rb) and Log(Zr/Fe) (Figure S10).

For the $CaCO_3$-free IRM$_{1T@AF\ 170mT}$, we only consider the measurement uncertainty of $CaCO_3$ and its propagation, since the measurement uncertainty of IRM$_{1T@AF\ 170mT}$ is so small that it is effectively negligible in this study. The predicted $CaCO_3$ (fractional value) is calculated by 0.096 * Ln(Ca/Fe) + 0.474, where the average fractional uncertainties of Ca and Fe ($\frac{\delta Ca}{Ca}$ and $\frac{\delta Fe}{Fe}$) are 0.002 and 0.007, respectively. The δLn(Ca/Fe) = sqrt (0.002^2 + 0.007^2) = 0.007, and the $\delta CaCO_3$ = 0.096 * δLn(Ca/Fe) = 0.001, following equation (iii). The $\delta CaCO_3$ can be considered as the δ(1- [$CaCO_3$]) based on equation (iii), and then the fractional uncertainty of (1- [$CaCO_3$]) (i.e., $\frac{\delta(1-[CaCO3])}{(1-[CaCO3])}$) is calculated and can be used as the fractional uncertainty of ([IRM$_{1T@AF\ 170mT}$] / (1- [$CaCO_3$])) (i.e., $\frac{\delta([IRM1T@AF\ 170mT]\ /\ (1-[CaCO3]))}{([IRM1T@AF\ 170mT]\ /\ (1-[CaCO3]))}$) based on equation (iv). Finally, the δ($CaCO_3$-free IRM$_{1T@AF\ 170mT}$), which is δ([IRM$_{1T@AF\ 170mT}$] / (1- [$CaCO_3$])), can be derived to obtain the 95 % (99 %) confidence intervals of $CaCO_3$-free IRM$_{1T@AF\ 170mT}$ using ± 1.96(2.58)δ (Figure S10).

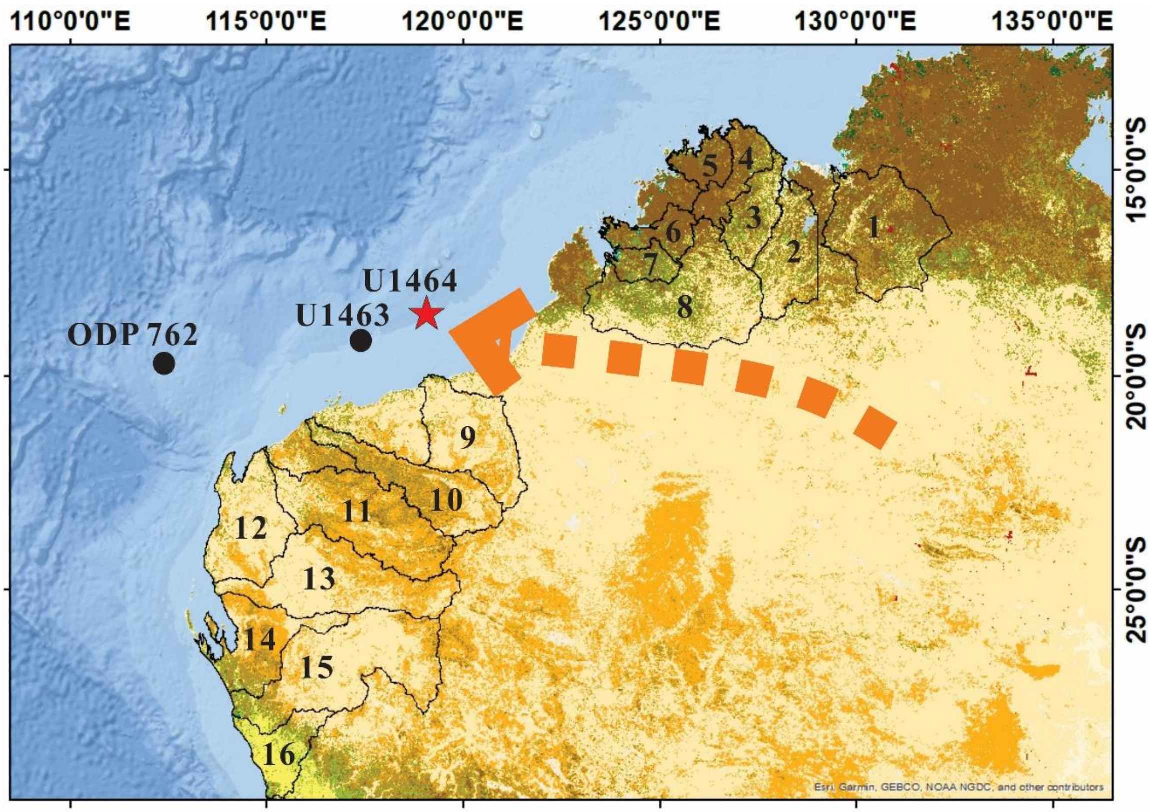

Figure S1. Northwest Australian river basins and locations of three cores (IODP Site U1464, U1463 and ODP site 762). Orange arrow indicates main aeolian dust path (after Bowler, 1976). Drainage basins of Victoria (1), Ord (2), Pentecost (3), Drysdale (4), King Edward (5), Isdell (6), Lennard (7), Fitzroy (8), De Grey (9), Fortescue (10), Ashburton (11), Lyndon-minilya (12), Gascoyne (13), Wooramel (14), Murchison (15), and Greenough (16) rivers (Australia's River Basins, 1997) are marked. Base map is from the GlobCover 2009 land cover and World Ocean Base in ArcGIS online.

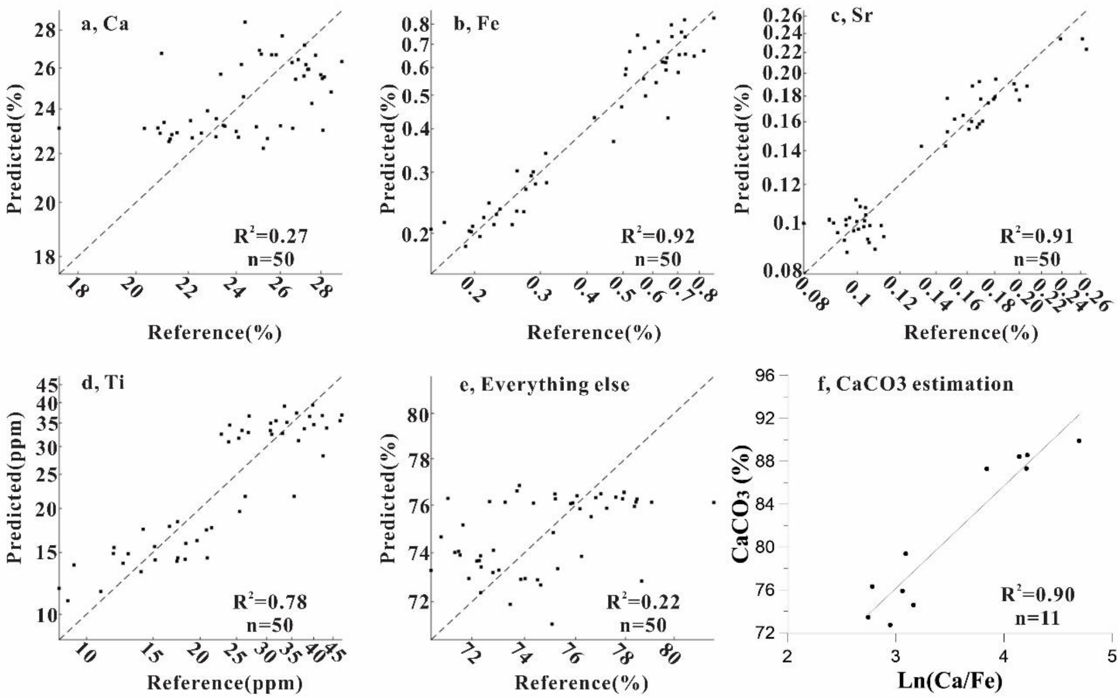

Figure S2. Reference versus predicted element concentrations for IODP Site U1464, based on ICP-OES and scanning XRF (a-e), using a multivariate log-ratio calibration model (Weltje et al., 2015). Shipboard $CaCO_3$ measurements versus Ln(Ca/Fe) for IODP Site U1464 (f) following the method of Liebrand et al., (2016).

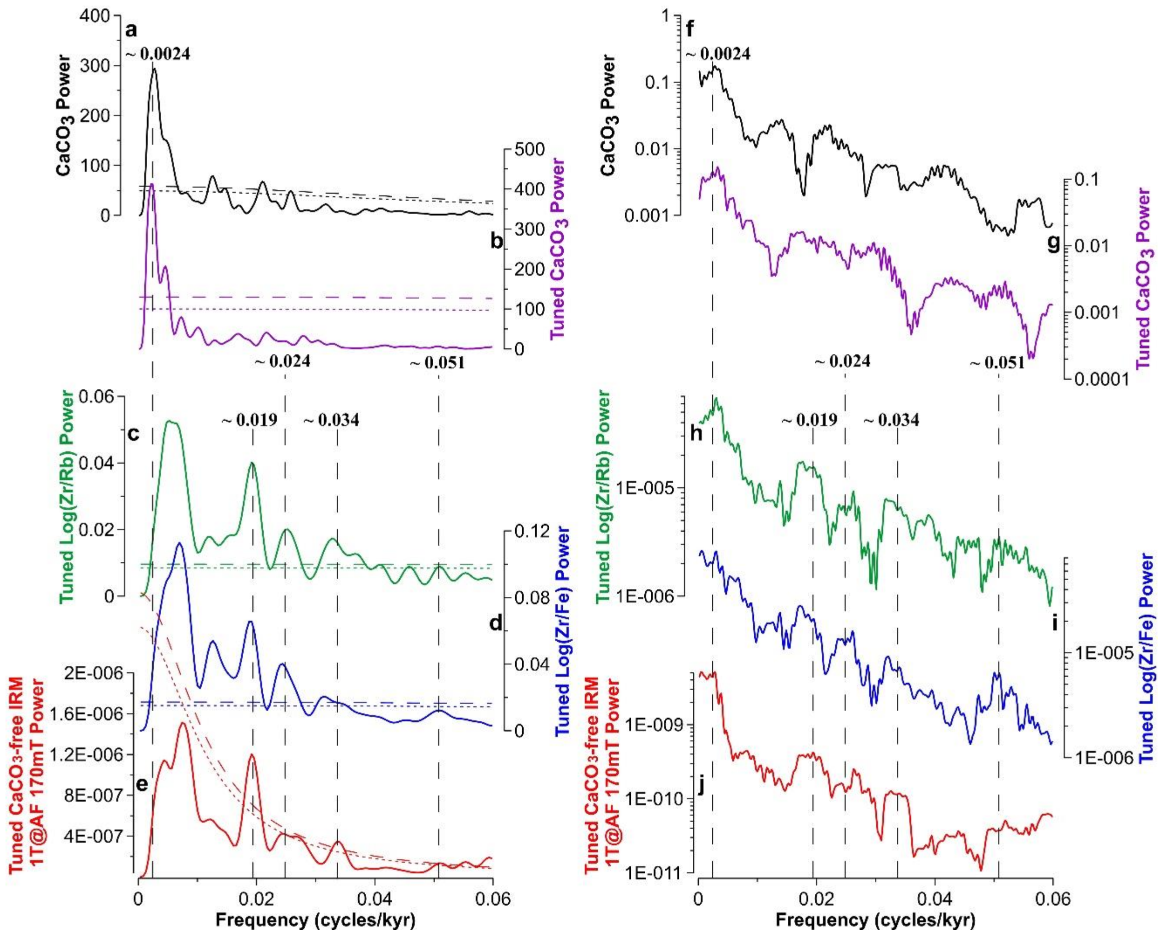

Figure S3. Spectral analyses of Site U1464 proxy records over the 1.6-2.9 Ma interval using the Redfit (a-e) and Multitaper (f-j) methods. Power spectra for $CaCO_3$ (a, f) on the biostratigraphy-based Bayesian model, and $CaCO_3$ (b, g), Log(Zr/Rb) (c, h), Log(Zr/Fe) (d, i) and $CaCO_3$-free $IRM_{1T@AF\ 170mT}$ (e, j) after eccentricity tuning. The a-e represent Redfit spectra with output parameters (oversample = 8, segment = 4 in a-b and oversample = 8, segment = 8 in c-e), and confidence levels (90%, dot; 95%, dashed) are indicated. The f-j represent Multitaper spectra with 5 tapers.

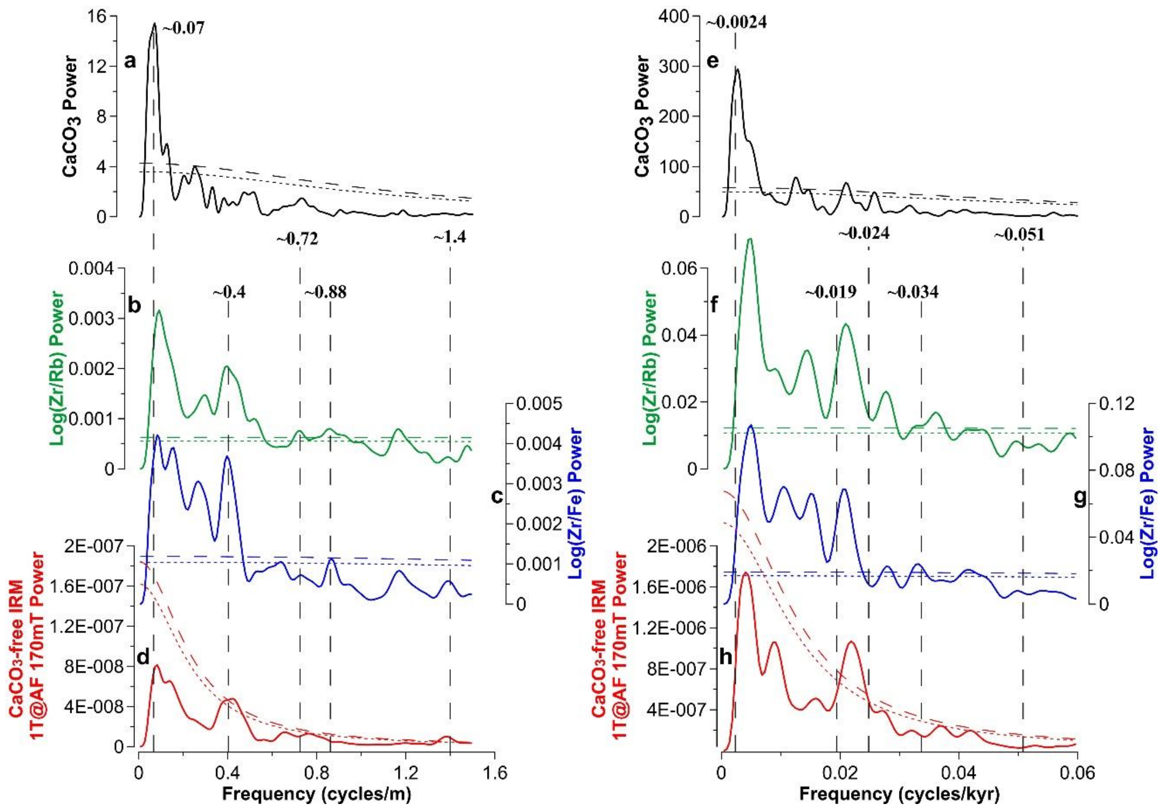

Figure S4. Spectral analyses of Site U1464 proxy records over the interval of ~47-108 mbsf (a-d) or ~1.6-2.9 Ma (e-h) using the Redfit method. Power spectra for $CaCO_3$ (a), Log(Zr/Rb) (b), Log(Zr/Fe) (c) and $CaCO_3$-free $IRM_{1T@AF\ 170mT}$ (d) on depth domain. Power spectra for $CaCO_3$ (e), Log(Zr/Rb) (f), Log(Zr/Fe) (g) and $CaCO_3$-free $IRM_{1T@AF\ 170mT}$ (h) on the biostratigraphy-based Bayesian model. The a-h represent Redfit spectra with output parameters (oversample = 8 and segment = 4 for $CaCO_3$ record; oversample = 8 and segment = 8 for dust proxy records), and confidence levels (90%, dot; 95%, dashed) are indicated.

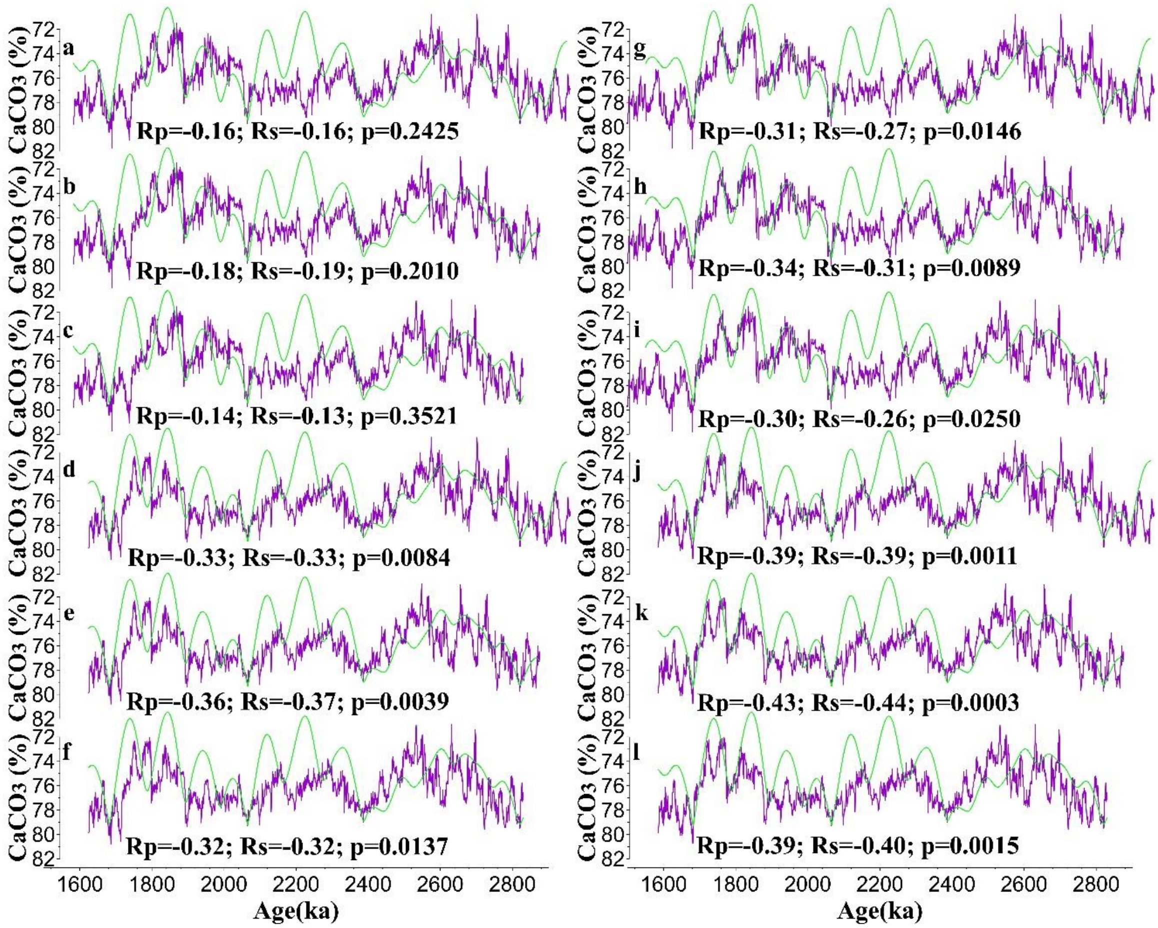

Figure S5. Alternative tunings for Site U1464 to eccentricity. Four eccentricity minima at 1682, 2066, 2388 and 2821 kyr are tuning targets for 12 potential $CaCO_3$ maxima. See Table S4 for tie-point depths used in (a)-(l). Option (k) is the choice in this study. Purple (green) lines represent $CaCO_3$ (eccentricity) records. Rp (Rs) represents Pearson (Spearman) correlation coefficient (see Text S1).

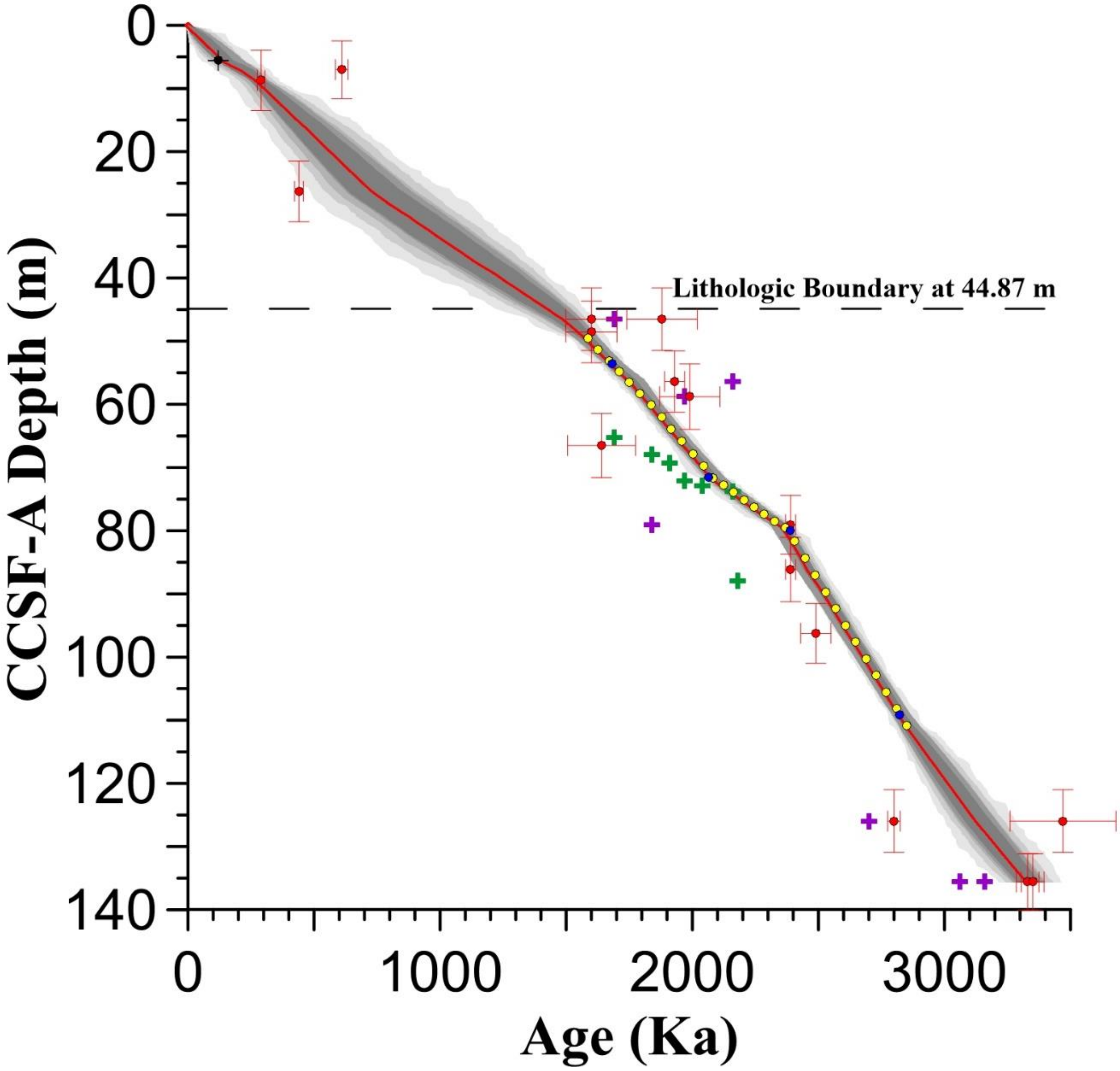

Figure S6. Same as main-text figure 2b, with additional age-depth markers for comparison. Green crosses are inferred chrono-stratigraphy for Site U1464 based on tie-points between U1463 and U1464 using dynamic time warping of natural gamma radiation records (Groeneveld et al., 2021). Purple crosses are revised biostratigraphic datums for neighboring Site U1463 from Groeneveld et al., 2021.

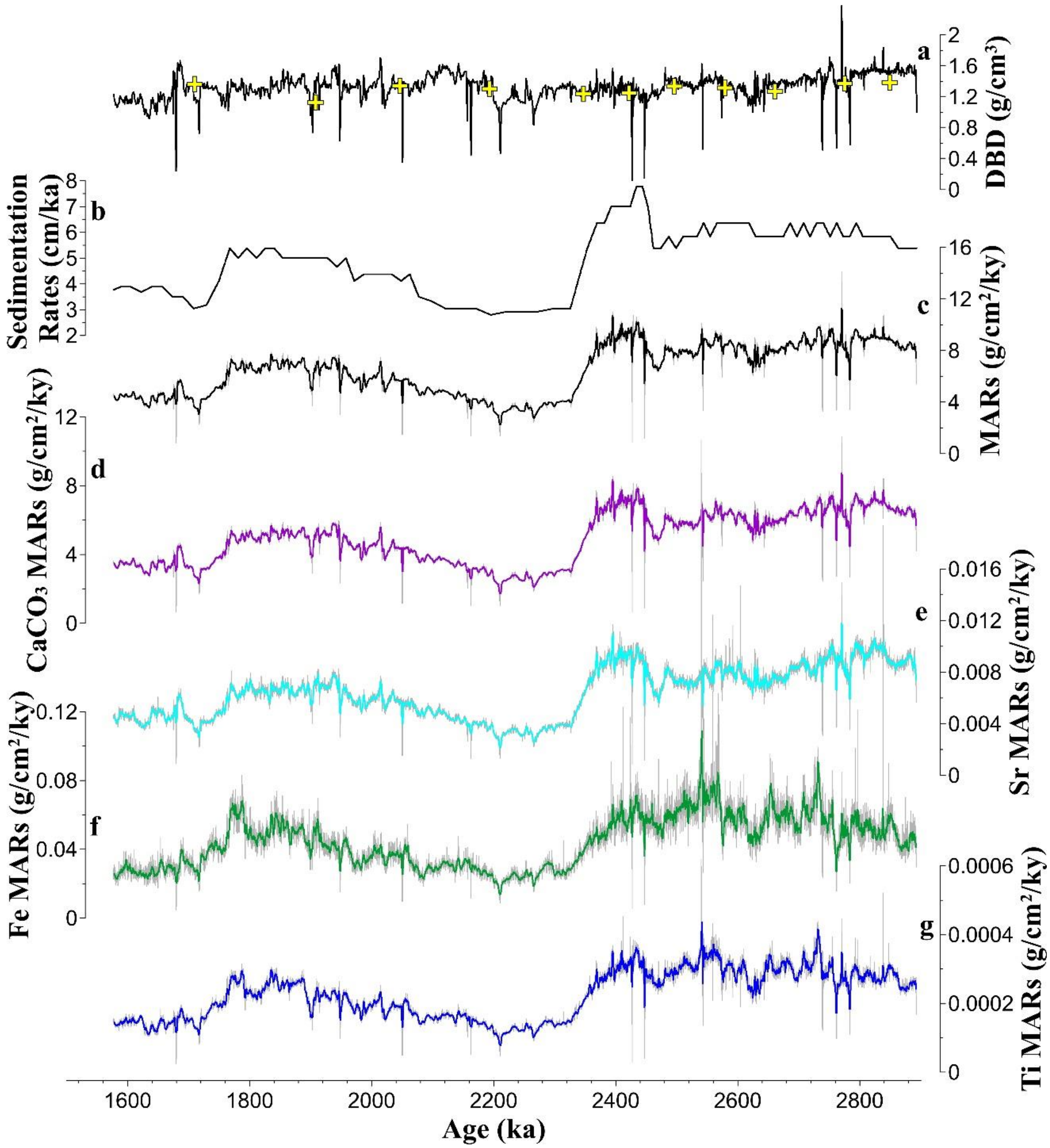

Figure S7. IODP Site U1464 sediment dry bulk density (DBD; black = calculated, yellow = shipboard measurements (Gallagher et al., 2017a), a), sedimentation rates (b) and mass accumulation rates (MARs) over ~1.6-2.9 Ma. Total MARs (c); $CaCO_3$ MARs (d); Sr MARs (e); Fe MARs (f) and Ti MARs (g). Bold lines (grey lines) in c-g are 21-point running averages (original data).

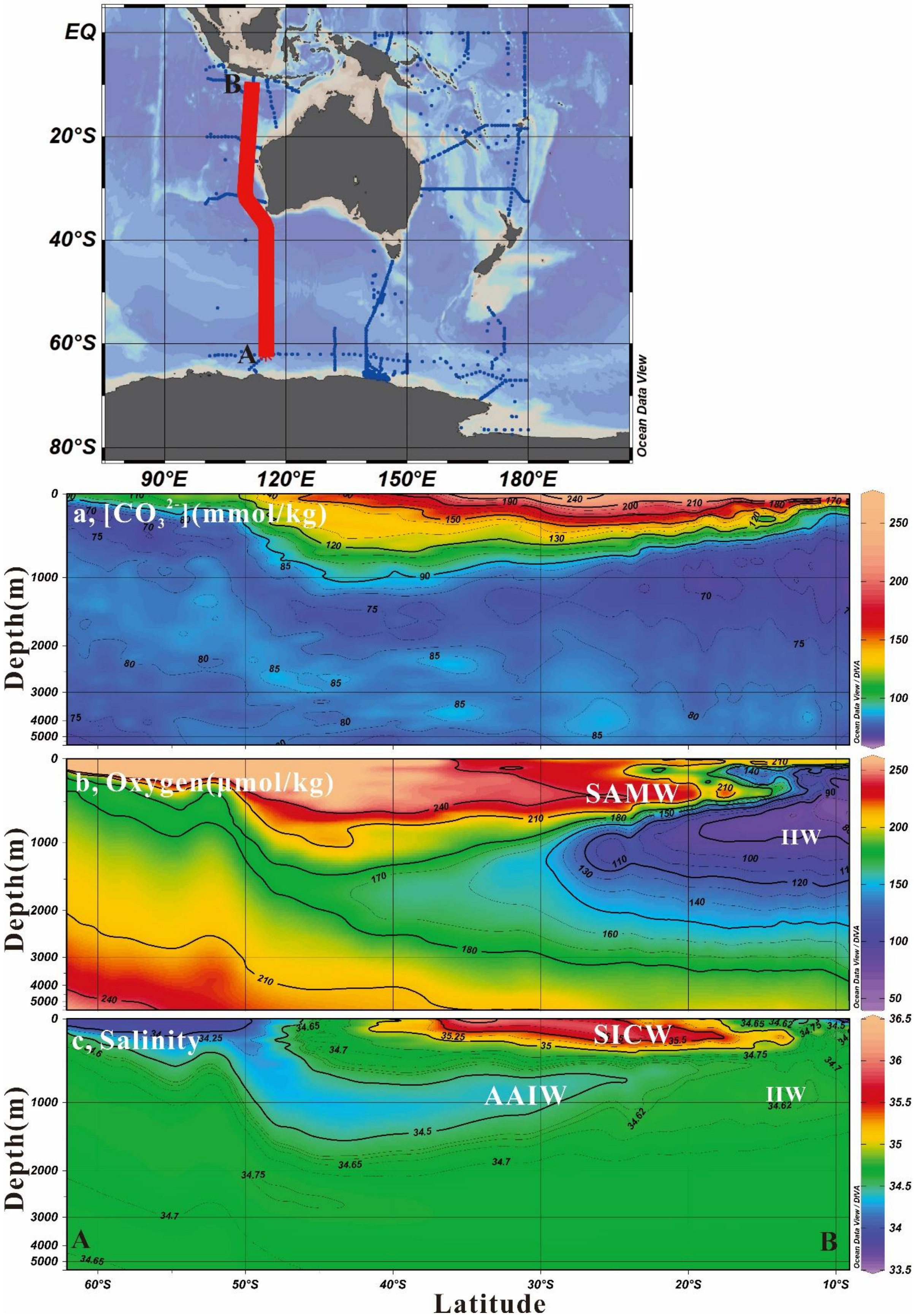

EQ
20°S
40°S
60°S
80°S
90°E
120°E
150°E
180°E
B
A
Ocean Data View
a, [CO_3^{2-}](mmol/kg)
Depth(m)
b, Oxygen(μmol/kg)
SAMW
IIW
c, Salinity
SICW
AAIW
IIW
A
B
60°S
50°S
40°S
30°S
20°S
10°S
Latitude

Figure S8. Meridional cross-section profiles of (a) $[CO_3^{2-}]$, (b) oxygen content and (c) salinity for transect-AB (red line). Data is from the GLODAPv2.2021 dataset (Key et al., 2015). $[CO_3^{2-}]$ from the GLODAPv2.2021 dataset is calculated using the CO2SYS method (Lewis & Wallace, 1998). Blue dots represent available data-points. SAMW: Sub-Antarctic Mode Water; AAIW: Antarctic Intermediate Water; SICW: South Indian Central Water; IIW: Indonesian Intermediate Water. SAMW is characterized by high-oxygen content (Herraiz-Borreguero & Rintoul, 2011; Woo & Pattiaratchi, 2008); AAIW is characterized by a salinity minimum (Wong, 2005; Woo & Pattiaratchi, 2008); SICW is characterized by a salinity maximum (Woo & Pattiaratchi, 2008); IIW is characterized by a salinity minimum (Talley & Sprintall, 2005) and an oxygen minimum (Fieux et al., 1996).

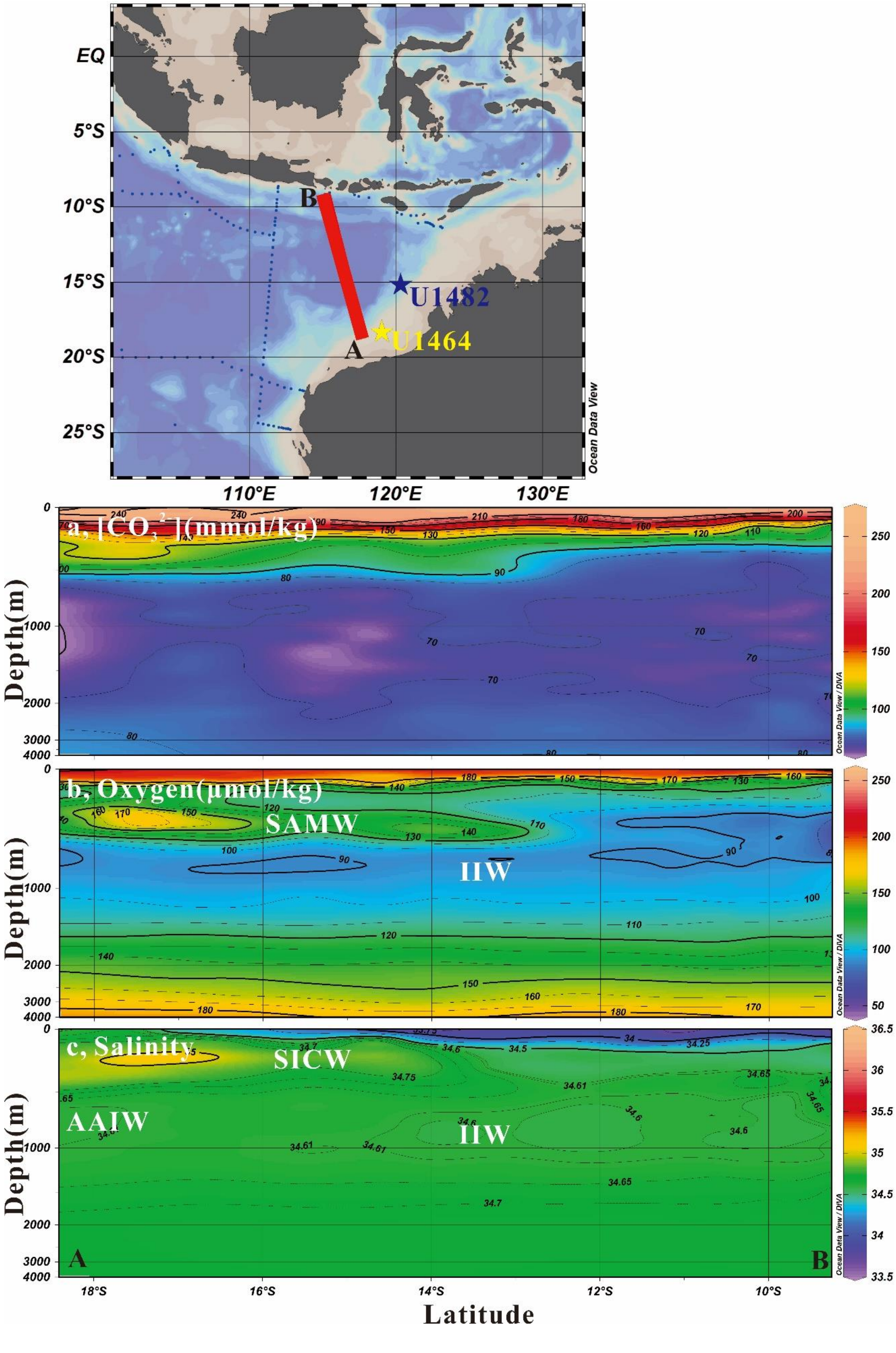
EQ
5°S
10°S
15°S
20°S
25°S
110°E
120°E
130°E
B
A
U1482
U1464
Ocean Data View
a, [CO_3^{2-}](mmol/kg)
b, Oxygen(μmol/kg)
SAMW
IIW
c, Salinity
SICW
AAIW
IIW
Depth(m)
Latitude
18°S
16°S
14°S
12°S
10°S
Ocean Data View / DIVA

Figure S9. Meridional cross-section profiles of (a) $[CO_3^{2-}]$, (b) oxygen content and (c) salinity for transect-AB (red line). Yellow (blue) star marks IODP Site U1464 (U1482). This cross-section is the closest GLODAPv2.2021 data to Site U1464 and Site U1482. $[CO_3^{2-}]$ from the GLODAPv2.2021 dataset is calculated using the CO2SYS method (Lewis & Wallace, 1998). Blue dots represent available data-points. SAMW: Sub-Antarctic Mode Water; AAIW: Antarctic Intermediate Water; SICW: South Indian Central Water; IIW: Indonesian Intermediate Water. SAMW is characterized by high-oxygen content (Herraiz-Borreguero & Rintoul, 2011; Woo & Pattiaratchi, 2008); AAIW is characterized by a salinity minimum (Wong, 2005; Woo & Pattiaratchi, 2008); SICW is characterized by a salinity maximum (Woo & Pattiaratchi, 2008); IIW is characterized by a salinity minimum (Talley & Sprintall, 2005) and an oxygen minimum (Fieux et al., 1996).

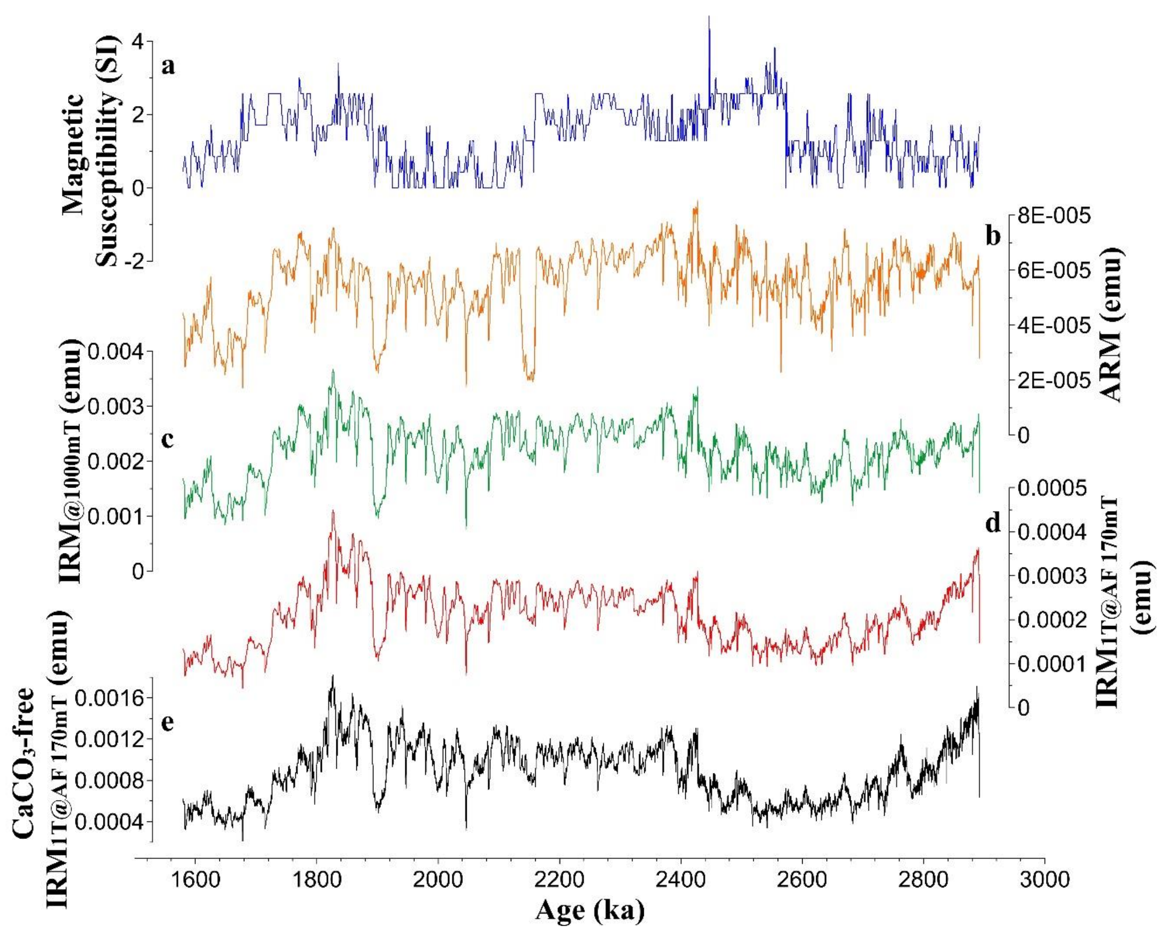

Figure S10. IODP Site U1464 magnetic parameters over the late Pliocene/early Pleistocene. (a) Magnetic susceptibility; (b) ARM; (c) $IRM_{@1000mT}$; (d) $IRM_{1T@AF\ 170mT}$ and (e) $CaCO_3$-free $IRM_{1T@AF\ 170mT}$. Magnetic susceptibility data is from Gallagher et al., 2017a and other data are measured in this study.

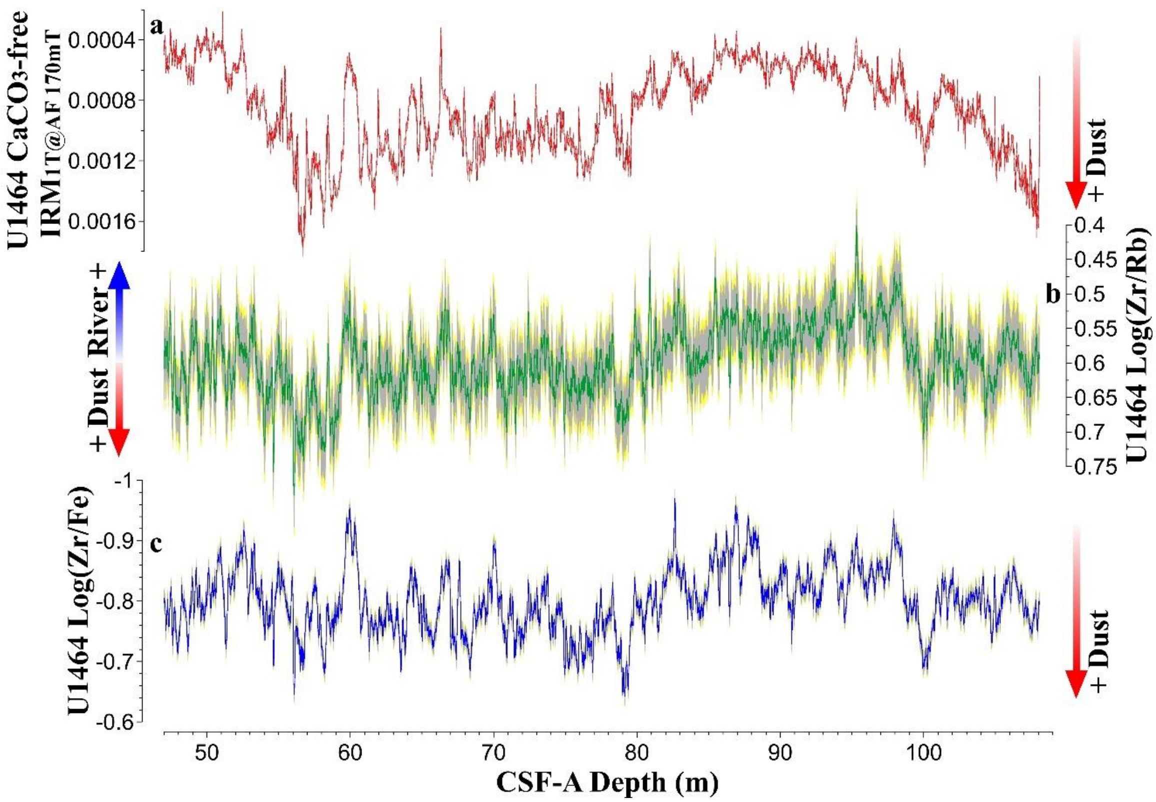

Figure S11. Dust proxy records from the Australian NWS and their uncertainties. $CaCO_3$-free $IRM_{1T@AF\ 170mT}$ (a, red), Log(Zr/Rb) (b, green: 21-point running average), and Log(Zr/Fe) (c, blue: 21-point running average) records at Site U1464. The grey and yellow shadings represent the 95 % and 99 % confidence intervals. Uncertainty calculations for these three dust records are shown in Text S2.

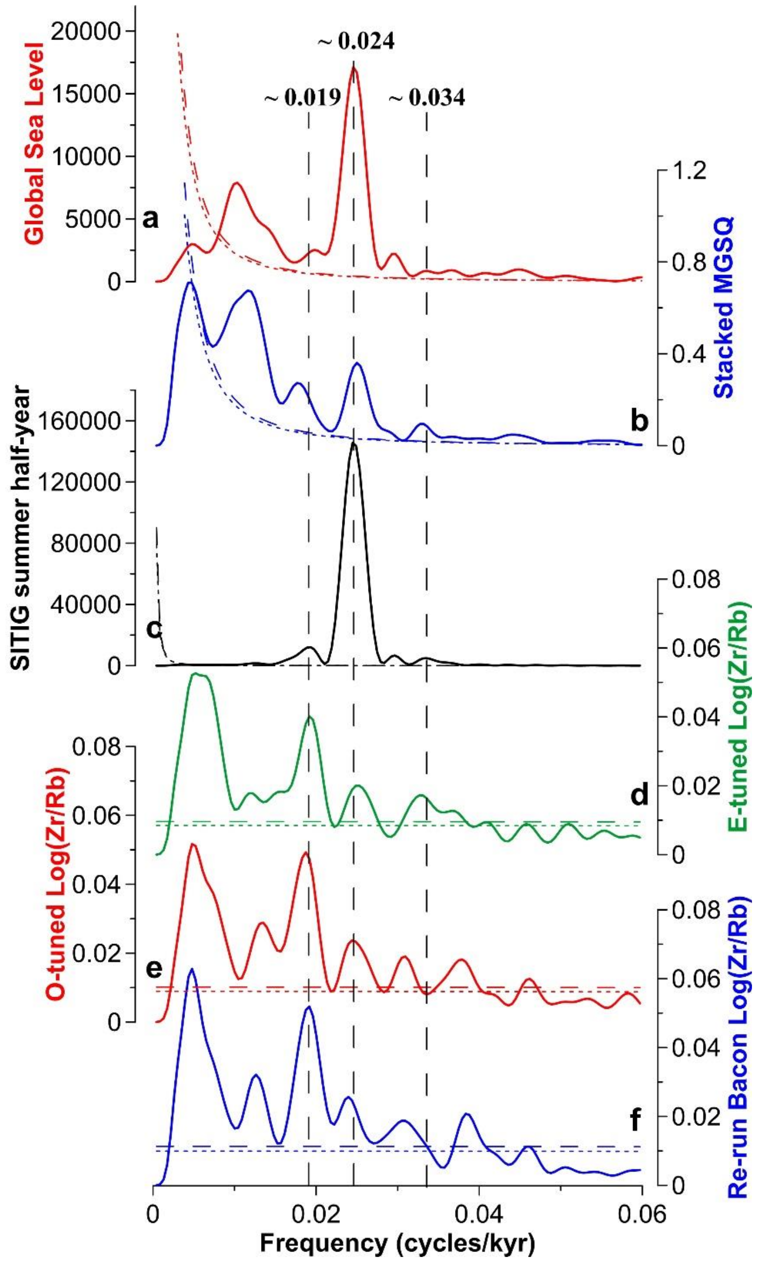

Figure S12. Spectral analyses of Northwest Australian dust fluxes and its three potential origins over the 1.6-2.9 Ma interval using the Redfit method. Power spectra for global sea level (Rohling et al., 2021) (a), stacked mean grain-size of quartz (MGSQ) from the Chinese Loess Plateau (Sun et al., 2006) (b), inter-tropical insolation gradient (SITIG) summer half-year (Laskar et al., 2004) (c), and Site U1464 Log(Zr/Rb) on the eccentricity tuning age model (d), obliquity tuning age model (e) and re-run Bacon age model (f). The Redfit spectra (oversample = 8, segment = 8) and confidence levels (90%, dashed; 95%, dot) are shown.

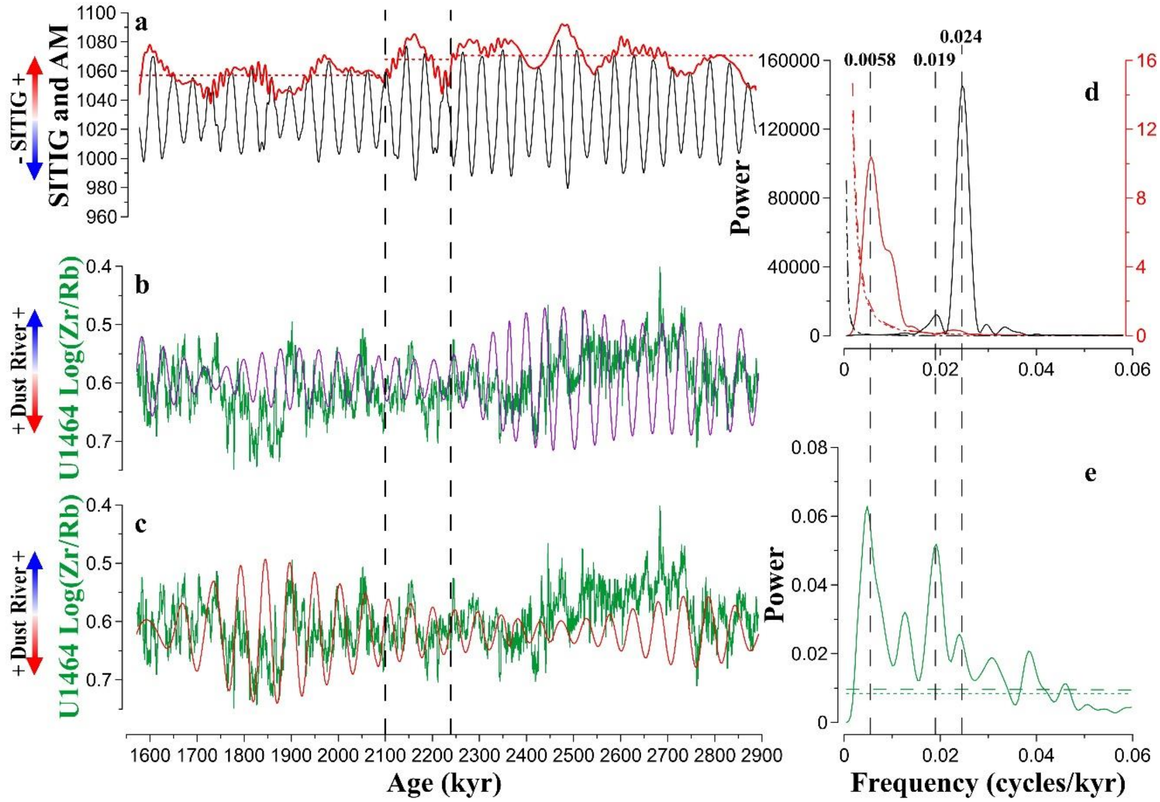

Figure S13. Inter-tropical insolation gradient (SITIG) summer half-year (black) and its amplitude modulation (AM, red) (a); Site U1464 Log(Zr/Rb) (green) and its 0.023-0.027 filter (purple) (b) and 0.017-0.021 filter (red) (c); Redfit power spectra of SITIG summer half-year (black) and its AM (red) (d), and Site U1464 Log(Zr/Rb) (green) (e). The SITIG summer half-year AM envelope is calculated using the MATLAB built-in function "hilbert" (Hilbert transform), and the mean values before 2.24 Ma, during 2.24-2.1 Ma and after 2.1 Ma are shown as red dotted lines in a. The Log(Zr/Rb) filters are calculated using the Fast Fourier transform in the Origin software package. Confidence levels (90%, dot; 95%, dashed) and significant frequencies (dash lines) in d and e are shown.

Table S1. Results of ICP-OES analysis for Site U1464, and standard deviation (SD) for certified reference materials (marine sediments BCSS-1, MESS-1 and estuarine sediments 1646).

Hole, Core, Section, Depth	CSF-A Depth/m	Ca/ppm	Fe/ppm	Sr/ppm	Ti/ppm
D1H1 36-37 cm	0.36	271791.19	2521.55	2385.06	8.46
D1H2 109-110 cm	2.59	260929.47	1891.64	2620.27	8.93
D2H1 78-79 cm	4.28	243912.04	2708.33	2666.67	10.92
D2H2 149-150 cm	6.49	271530.51	3100.39	2066.93	15.15
D2H4 1-2 cm	8.01	242292.39	3117.85	1685.73	20.90
D2H6 17-18 cm	11.17	268626.98	1958.71	1469.04	11.78
D2H7 65-66 cm	12.87	273355.58	2287.89	1572.93	18.33
D3H1 144-145 cm	14.44	273812.92	2592.59	1709.40	19.63
D3H3 142-143 cm	17.42	280691.51	2599.91	1630.00	16.60
D3H4 144-145 cm	18.94	281755.47	2911.51	1669.84	21.47
D3H5 140-141 cm	20.4	279954.03	2742.59	1685.39	14.13
D3H7 53-54 cm	22.05	267369.15	2869.38	1611.86	17.42
D4H2 70-71 cm	24.7	233333.33	2835.28	1516.03	20.79
D4H3 62-63 cm	26.12	277248.93	1934.79	1956.21	9.27
D4H4 149-150 cm	28.49	209504.90	2115.83	1793.55	12.91
D4H5 77-78 cm	29.27	255956.59	2067.14	1696.11	15.20
D4H7 60-61 cm	32	251155.27	1975.51	1802.22	17.37
D5H2 117-118 cm	34.67	290882.92	2252.88	2000.96	18.25
D5H4 18-19 cm	36.68	265655.62	2183.85	1973.87	17.46
D5H6 20-21 cm	39.7	250397.20	1528.04	1808.41	13.95
D5H7 56-57 cm	41.56	258108.11	1657.82	1636.10	12.50
D6H2 1-2 cm	43.01	272419.43	2340.03	1751.52	11.83
D6H3 0-1 cm	44.5	243153.92	4185.55	1458.92	26.35
D6H3 53-54 cm	45.03	285259.99	4712.08	1469.70	25.45
D6H4 56-57 cm	46.56	275391.50	6590.60	1315.44	35.50
D6H4 146-147 cm	47.46	210471.83	5069.81	794.42	25.83
D6H5 87-88 cm	48.37	280966.42	7023.59	952.81	30.72
D6H6 61-62 cm	49.61	265960.04	6374.27	994.15	23.82
D6H6 147-148 cm	50.47	248979.10	6504.62	1035.49	25.33
D7H1 80-81 cm	51.8	231312.17	7162.48	952.16	40.03
D7H2 5-6 cm	52.55	252171.95	8748.87	1004.52	42.15
D7H3 1340 cm	55.34	213450.02	6729.62	967.30	33.98
D7H4 147-148 cm	56.97	212837.54	6752.99	956.18	39.73
D7H6 59-60 cm	59.09	221516.96	7328.14	1044.91	36.04
D8H1 145-146 cm	61.95	260158.80	6130.31	1106.96	30.97
D8H3 2-3 cm	63.52	220878.58	5671.27	1036.53	36.44
D8H3 145-146 cm	64.95	234390.13	6512.58	1030.98	26.85
D8H6 1-2 cm	68.01	231451.21	5742.94	1054.98	22.78
D8H7 27-28 cm	69.77	215530.67	7339.34	1051.61	39.01
D9H2 117-118 cm	72.67	241003.83	6201.62	918.76	26.98
D9H4 17-18 cm	74.67	225276.83	5704.86	983.82	31.78
D9H5 2-3 cm	76.02	235133.89	5090.03	886.43	33.07
D9H6 81-82 cm	78.31	240009.40	7066.29	902.68	23.95
D10H1 100-101 cm	80.5	208100.83	6549.19	1027.90	43.27
D10H3 42-43 cm	82.92	173891.74	8224.45	1119.93	46.95
D10H5 34-35 cm	85.84	212358.44	7304.28	945.35	33.46
D11H2 8-9 cm	90.58	208958.62	5463.85	886.77	30.76
D11H5 28-29 cm	95.28	253995.27	7751.77	1078.01	47.50
D12H1 140-141 cm	99.9	227825.89	4956.70	1011.85	42.33
D12H5 101-102 cm	105.51	203052.39	5207.29	997.72	37.78
Certified Reference Materials	**Replicates Count**	**Ca SD**	**Fe SD**	**Sr SD**	**Ti SD**
1646	4	3.422‰	1.064‰	0.008‰	0.004‰
BCSS-1	3	4.981‰	2.607‰	0.009‰	0.005‰
MESS-1	3	2.445‰	2.792‰	0.004‰	0.022‰
Average Value	---	3.616‰	2.154‰	0.007‰	0.010‰

Table S2. IODP Site U1464 shipboard $CaCO_3$ measurements (Gallagher et al., 2017a), scanning-XRF Ln(Ca/Fe) values, and predicted $CaCO_3$ content.

Hole, Core, Section	CSF-A Depth/m	$CaCO_3$/%	Ln(Ca/Fe)	Predicted $CaCO_3$/%
B1H1	1.45	89.91	4.693	92.35
B3H3	16.15	88.42	4.140	87.05
B4H3	25.55	87.32	4.207	87.70
B5H4	36.68	88.57	4.213	87.75
B6H3	44.65	87.30	3.839	84.17
B7H3	54.15	73.45	2.746	73.70
B7H3	63.65	75.90	3.062	76.72
B7H3	73.15	72.72	2.949	75.64
B7H3	82.65	76.31	2.784	74.07
B7H3	92.15	74.59	3.164	77.70
B7H3	101.65	79.38	3.093	77.03

Table S3. Age control-points (Gallagher et al., 2017a) in our Site U1464 Bacon age model. CN: calcareous nannofossils; PF: planktonic foraminifers; Base: first appearance depth; Top: last appearance depth. The CCSF-A for each point is calculated from their middle CSF-A depth, based on the established linear relationship between CSF-A and CCSF-A (Gallagher et al., 2017a).

Hole, Core, Section	Depth CSF-A (m)	Depth CCSF-A (m)	Marker Species	Type	Age (Ma)
Core Top	0	0	---	---	0
U1464D-1H-CC	3.55	8.72	Base E. huxleyi	CN	0.29
U1464B-2H-CC	11.51	7.02	Top G. tosaensis	PF	0.61
U1464B-4H-CC	30.82	26.28	Top P. lacunosa	CN	0.44
---	43.00	44.87	Lithologic Boundary	---	---
U1464B-6H-CC	49.82	46.53	Top C. macintyrei	CN	1.6
U1464B-6H-CC	49.82	46.53	Top G. fistulosus	PF	1.88
U1464B-6H-CC	49.82	56.37	Base G. truncatulinoides	PF	1.93
U1464D-6H-CC	51.33	48.54	Top C. macintyrei	CN	1.6
U1464B-7H-CC	59.46	56.37	Top D. brouweri	CN	1.93
U1464D-7H-CC	60.84	58.78	Top G. extremus	PF	1.99
U1464B-8H-CC	69.09	66.51	Top G. apertura	PF	1.64
U1464D-9H-CC	79.83	79.04	Top G. limbata	PF	2.39
U1464B-10H-CC	88.17	86.14	Top D. pentaradiatus	CN	2.39
U1464B-11H-CC	97.42	96.23	Top D. surculus	CN	2.49
U1464B-14H-CC	126.30	125.96	Top D. tamalis	CN	2.8
U1464B-14H-CC	126.30	135.59	Base G. fistulosus	PF	3.33
U1464B-14H-CC	126.30	135.59	Base G. tosaensis	PF	3.35
U1464B-14H-CC	126.30	125.96	Top D. altispira	PF	3.47

Table S4. Different depth options for each Site U1464 $CaCO_3$-to-eccentricity tie-point (see Figure 4; Figure S5). Twelve possible combinations are shown (Figure S5). Bold numbers represent the best option for the U1464 age model in this study, based on visual alignment and correlation analysis between eccentricity and U1464 $CaCO_3$.

Eccentricity Tuning-point	Tuning Age (kyr)	Depth (m CCSF-A)	Bacon Age (kyr)
1	1682	51.99	1746
1	**1682**	**53.62**	**1800**
2	2066	63.05	2012
2	**2066**	**71.57**	**2174**
3	**2388**	**79.97**	**2332**
4	2821	104.91	2738
4	**2821**	**109.18**	**2817**
4	2821	112.22	2873

Table S5. IODP Site U1464 tuning tie-points.

Depth (m CCSF-A)	Initial Bacon Age (kyr)	Tuning Age (kyr)	Reference proxy	Orbital Target
49.53	1664	1587	Log(Zr/Rb)	Obliquity
51.33	1725	1627	Log(Zr/Rb)	Obliquity
53.14	1784	1672	Log(Zr/Rb)	Obliquity
53.62	1800	1682	$CaCO_3$	Eccentricity
54.85	1841	1709	Log(Zr/Rb)	Obliquity
56.52	1892	1750	Log(Zr/Rb)	Obliquity
58.28	1926	1793	Log(Zr/Rb)	Obliquity
60.10	1958	1837	Log(Zr/Rb)	Obliquity
62.00	1993	1878	Log(Zr/Rb)	Obliquity
63.93	2028	1917	Log(Zr/Rb)	Obliquity
65.88	2063	1959	Log(Zr/Rb)	Obliquity
67.80	2100	2002	Log(Zr/Rb)	Obliquity
69.80	2139	2044	Log(Zr/Rb)	Obliquity
71.57	2174	2066	$CaCO_3$	Eccentricity
71.71	2177	2081	Log(Zr/Rb)	Obliquity
72.82	2198	2124	Log(Zr/Rb)	Obliquity
73.94	2220	2164	Log(Zr/Rb)	Obliquity
75.14	2244	2205	Log(Zr/Rb)	Obliquity
76.30	2266	2246	Log(Zr/Rb)	Obliquity
77.41	2288	2284	Log(Zr/Rb)	Obliquity
78.48	2309	2327	Log(Zr/Rb)	Obliquity
79.55	2327	2368	Log(Zr/Rb)	Obliquity
79.97	2332	2388	$CaCO_3$	Eccentricity
81.61	2354	2405	Log(Zr/Rb)	Obliquity
84.35	2390	2448	Log(Zr/Rb)	Obliquity
87.06	2429	2487	Log(Zr/Rb)	Obliquity
89.749	2473	2528	Log(Zr/Rb)	Obliquity
92.36	2515	2569	Log(Zr/Rb)	Obliquity
95.05	2559	2607	Log(Zr/Rb)	Obliquity
97.64	2604	2649	Log(Zr/Rb)	Obliquity
100.28	2653	2690	Log(Zr/Rb)	Obliquity
102.90	2701	2728	Log(Zr/Rb)	Obliquity
105.52	2750	2768	Log(Zr/Rb)	Obliquity
108.21	2799	2810	Log(Zr/Rb)	Obliquity
109.18	2817	2821	$CaCO_3$	Eccentricity
110.88	2848	2851	Log(Zr/Rb)	Obliquity